

# Investigating the Photochemical Decomposition of Solid 1,3,5-Trinitro-1,3,5-triazinane (RDX)

Santosh K. Singh, Vasant Vuppuluri, Steven F. Son, and Ralf I. Kaiser\*

Cite This: *J. Phys. Chem. A* 2020, 124, 6801–6823

Read Online

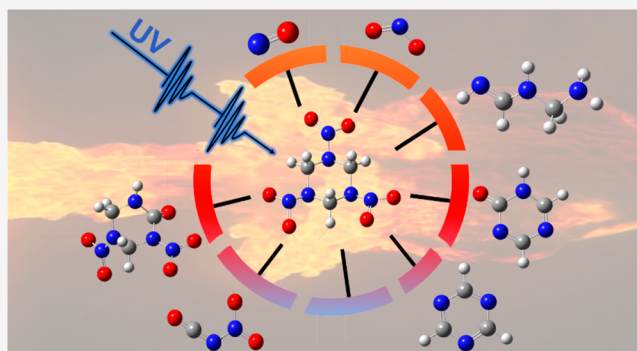
ACCESS |

Metrics &amp; More

Article Recommendations

Supporting Information

**ABSTRACT:** Energetic materials such as 1,3,5-trinitro-1,3,5-triazinane (RDX) are known to photodissociate when exposed to UV light. However, the fundamental photochemical process(es) that initiate the decomposition of RDX is (are) still debatable. In this study we investigate the photodissociation of solid-phase RDX at four distinct UV wavelengths (254 nm (4.88 eV), 236 nm (5.25 eV), 222 nm (5.58 eV), 206 nm (6.02 eV)) exploiting a surface science machine at 5 K. We also conducted dose-dependent studies at the highest and lowest photon energy of 206 nm (6.02 eV) and 254 nm (4.88 eV). The products were monitored online and *in situ* via infrared spectroscopy. During the temperature-programmed desorption phase, the subliming products were detected with a reflectron time-of-flight mass spectrometer coupled with soft-photoionization at 10.49 eV (PI-ReTOF-MS). Infrared spectroscopy revealed the formation of small molecules including nitrogen monoxide (NO), nitrogen monoxide dimer ( $[\text{NO}]_2$ ), dinitrogen trioxide ( $\text{N}_2\text{O}_3$ ), carbon dioxide ( $\text{CO}_2$ ), carbon monoxide (CO), dinitrogen monoxide ( $\text{N}_2\text{O}$ ), water ( $\text{H}_2\text{O}$ ), and nitrite group ( $-\text{ONO}$ ) while ReTOF-MS identified 32 cyclic and acyclic products. Among these, 11 products such as nitril isocyanate ( $\text{CN}_2\text{O}_3$ ), 5-nitro-1,3,5-triazinan-2-one ( $\text{C}_3\text{H}_6\text{N}_4\text{O}_3$ ) and 1,5-dinitro-1,3,5-triazinan-2-one ( $\text{C}_3\text{H}_5\text{N}_5\text{O}_5$ ) were detected for the first time in photodecomposition of RDX. Dose-dependent in combination with wavelength-dependent photolysis experiments aid to identify key primary and secondary products as well as distinguished pathways that are more preferred at lower and higher photon energies. Our experiments revealed that N–NO<sub>2</sub> bond fission and nitro–nitrite isomerization are the initial steps in the UV photolysis of RDX. Reaction mechanisms are derived by comparing the experimental findings with previous electronic structure calculations to rationalize the origin of the observed products. The present study can assist in understanding the complex chemistry behind the photodissociation of electronically excited RDX molecule, thus bringing us closer to unraveling the decomposition mechanisms of nitramine-based explosives.

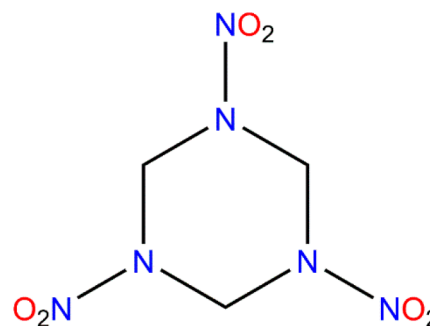


## 1. INTRODUCTION

Cyclic nitramines, such as 1,3,5-trinitro-1,3,5-triazinane (RDX), have wide applications as explosives and rocket propellants due to their high energy content.<sup>1–3</sup> Therefore, an understanding of the fundamental decomposition mechanisms of energetic materials at the molecular level is essential to increase the energy efficiency of nitramines in explosion and combustion applications. Over the past decades, copious studies have been devoted to investigate the fundamental chemical processes involved in the fragmentation of RDX (Scheme 1).<sup>1–43</sup> Diverse methods ranging from shock waves, infrared (IR) lasers, electron beams to ultraviolet (UV) lasers have been employed to initiate the complex dissociation mechanism(s), but the very first reaction step(s) that initialize the decomposition is (are) still debated.<sup>4,8–15</sup>

The decomposition of condensed phase RDX via thermal energy, shock waves, and infrared laser exposure suggest that the N–NO<sub>2</sub> bond fission represents the primary pathway.<sup>8,13,14</sup> On the contrary, infrared multiphoton dissociation of RDX in molecular beams in the gas phase reveals a triple C–N bond

Scheme 1. Molecular Structure of 1,3,5-Trinitro-1,3,5-triazinane (RDX)



Received: June 23, 2020

Revised: July 27, 2020

Published: July 28, 2020



rupture leading to three methylene nitramine molecules ( $\text{H}_2\text{C}=\text{N}-\text{NO}_2$ ) as the dominating channel.<sup>10</sup> This channel has also been observed in the decomposition of solid phase RDX via infrared laser leading eventually to the formation of ketene ( $\text{H}_2\text{CCO}$ ) and water ( $\text{H}_2\text{O}$ ).<sup>44</sup> Thermal decomposition studies disclose yet another primary mechanism, which involves a concerted elimination of nitrous acid (HONO) along with the formation of triazine ( $\text{C}_3\text{H}_3\text{N}_3$ ).<sup>8,9,41</sup> Very recently, the dissociation of RDX conducted via energetic electrons revealed that the products involving the  $\text{N}-\text{NO}_2$  homolysis and HONO elimination are more prevailing than the triple dissociation.<sup>15</sup> Although several discrepancies revolve around the initial step of decomposition, the proposed reaction schemes in the aforementioned studies could elucidate the decomposition of RDX from its ground electronic state ( $S_0$ ). However, the primary/secondary steps responsible for the fragmentation of nitramine-based energetic materials from their excited electronic states could be quite different.<sup>5,6</sup>

Previous experiments demonstrated that excited electronic states ( $S_1$ ,  $S_2$ ) of energetic materials could play a fundamental role in their decomposition and also in the ignition processes. In the laboratory, these excited states are readily accessible once the sample is exposed to ultraviolet (UV) photons.<sup>5,45</sup> However, only a few studies have been pursued to unravel the fragmentation processes of RDX that occur after electronic excitation (Table S1).<sup>4,16,23,25,26,28</sup> Here, the majority of the UV photolysis experiments are conducted in the gas phase by Bernstein and co-workers.<sup>4–7</sup> These studies investigated the photodissociation of RDX from its excited electronic states upon photoexcitation at three distinct wavelengths of 230, 228, and 226 nm; in each case, only nitrogen monoxide (NO) was observed.<sup>4</sup> Their observation of rotationally cold, but vibrationally hot excitation spectra of NO (nitrogen monoxide) suggests that RDX dissociates in the  $S_0$  state after rapid internal conversion from the  $S_1$  state.<sup>46</sup> Calculations on the excited-state potential energy surface (PES) revealed that following electronic excitation, the RDX molecules undergo nitro–nitrite isomerization after passing through a series of conical intersections (CIs) and finally dissociate from the  $S_0$  state via simple O–NO bond rupture processes.<sup>7</sup> Im et al. conducted femtosecond pump–probe experiments to demonstrate that photodecomposition dynamics of RDX at 226 nm involves a time scale faster than 180 fs.<sup>6</sup> Lemire et al. also conducted photodissociation of RDX at 226 nm in the gas phase and primarily observed only the nitrogen monoxide (NO) fragment.<sup>27</sup>

Although gas phase studies by Bernstein and co-workers convincingly suggested nitro–nitrite isomerization to be a major fragmentation channel involving initially excited state dynamics, evidence of such isomerization mechanism upon photoexcitation has not been observed in the condensed phase yet. The infrared spectrum of RDX collected by Alix et al. in the argon matrix at 10 K after photodissociation with a broadband UV light did not reveal any vibrational features corresponding to the nitrite group ( $-\text{ONO}$ ). Only features attributed to nitrogen monoxide (NO), formaldehyde ( $\text{H}_2\text{CO}$ ), dinitrogen monoxide ( $\text{N}_2\text{O}$ ), carbon monoxide (CO), dinitrogen trioxide ( $\text{N}_2\text{O}_3$ ), methane ( $\text{CH}_4$ ), and ozone ( $\text{O}_3$ ) were reported.<sup>16</sup> Gares et al. recorded the deep-ultraviolet resonance Raman (DUVRR) spectra of solution and solid phase RDX after photolysis at 229 nm (5.41 eV) and observed a decrease in the  $\text{N}-\text{NO}_2$  band intensity along with evidence of the formation of nitrate ion ( $-\text{NO}_3^-$ ) and carbon

nitrides ( $\text{C}\equiv\text{N}$ ) moieties.<sup>25</sup> However, no vibrational signature of nitrite group ( $-\text{ONO}$ ) or nitrogen dioxide ( $\text{NO}_2$ ) were reported; therefore, the authors predicted that the  $\text{N}-\text{NO}_2$  bond cleavage represents the dominant pathway. Tang et al. also proposed the  $\text{N}-\text{NO}_2$  bond fission as a primary step in the dissociation of solid RDX at 266 nm (4.66 eV) based on the detected products such as  $\text{NO}_2$  (nitrogen dioxide), NO (nitrogen monoxide), and (a)cyclic species carrying  $\text{C}=\text{N}$  moieties.<sup>23</sup>

In summary, previous UV photolysis studies have not elucidated the role of the nitro–nitrite isomerization mechanism in the decomposition of RDX. This is due to the lack of the identification of higher molecular weight products that could result from the nitro–nitrite isomerization process. In the gas phase, the higher molecular weight species formed via the nitro–nitrite isomerization plus nitrogen monoxide (NO) elimination could be undetected considering the low number densities and absence of (state) specific detection schemes such as laser induced fluorescence (LIF) and resonance enhanced multiphoton ionization (REMPI); this is evident from the works of Bernstein et al. reporting solely NO (nitrogen monoxide) as the primary product, whose LIF scheme is well established, but no heavier cofragments.<sup>5</sup> On the other hand, condensed phase studies could provide a significantly more complex chemistry (Table S1).<sup>16,26</sup> However, a systematic experimental approach is required to shed fundamental insight on the complex chemistry of the decomposition of RDX upon UV photo fragmentation, i.e., pathways which may involve multiple reaction channels such as  $\text{N}-\text{NO}_2$  bond fission, nitro–nitrite isomerization, and/or HONO elimination. Furthermore, a complete spectrum of the wavelength-dependent photodissociation products of RDX in the condensed phase is scarce.

Herein, we investigate the photofragmentation of solid RDX at four distinct UV wavelengths (254 nm (4.88 eV), 236 nm (5.25 eV), 222 nm (5.58 eV), and 206 nm (6.02 eV)) exploiting a surface science machine at 5 K to trap the products within the low temperature solid. These energies are well below the adiabatic ionization energy of RDX determined to be between 9.9 and 10.2 eV in the gas phase.<sup>47,48</sup> At the highest and lowest photon energy of 206 nm (6.02 eV) and 254 nm (4.88 eV), we also conducted time (dose) dependent studies to gauge the effects of higher order reaction products. By employing four different wavelengths, distinct electronic transitions of RDX, i.e.,  $n \rightarrow \pi^*$  and  $\pi_R \rightarrow \pi^*$  are accessed.<sup>49,50</sup> The weak  $n \rightarrow \pi^*$  transition involves an excitation of a nonbonding electron located at the oxygen atom and can be excited via 254 nm (4.88 eV) and 222 nm (5.58 eV). The significantly stronger  $\pi_R \rightarrow \pi^*$  absorption promotes an electron located in the  $\pi$  orbital of the ring-nitrogen to the  $\pi^*$  orbital at the  $\text{NO}_2$  group. The 236 nm (5.25 eV) and 206 nm (6.02 eV) excitation can readily activate this  $\pi_R \rightarrow \pi^*$  transition.<sup>50</sup> The calculated oscillator strengths of these transitions are provided in Table 1.

Thus, the discrete choice of excitation wavelengths enables us to cover critical and major transitions that populate the electronic spectrum of RDX. During the photolysis, chemical changes in the RDX samples were monitored via Fourier transform infrared spectroscopy (FTIR). A reflectron time-of-flight mass spectrometry coupled with VUV photoionization (PI-ReTOF-MS) was employed to record the mass spectra of the photoirradiated samples during temperature-programmed desorption (TPD) following the photolysis of the RDX. Our

**Table 1.** Calculated Transition Energies ( $\Delta E$ ) and Gas Phase Oscillator Strengths ( $f$ ) of the Excited States of RDX Probed in This Study

wavelength (nm)	photon energy (eV)	calculated (RI-CC2/TZVPP) <sup>a</sup>			
		state	transition	transition energy ( $\Delta E$ , eV)	oscillator strength ( $f$ )
254	4.88	1E	$n \rightarrow \pi^*$	4.54	0.000
236	5.25	2E	$\pi_R \rightarrow \pi^*$	5.24	0.064
222	5.58	1A <sub>1</sub>	$n \rightarrow \pi^*$	5.36	0.025
206	6.02	2A <sub>1</sub>	$\pi_R \rightarrow \pi^*$	6.01	0.126

<sup>a</sup>Values reproduced from ref 50.

experiments revealed a wide spectrum of photoproducts of RDX. The FTIR spectroscopy detects small decomposition products and the nitrite (-ONO) functional group, while the majority of higher-order products including 32 cyclic and acyclic products were identified through PI-ReTOF-MS. Among these, 11 products observed at  $m/z$  values of 59 ( $C_2H_5NO$ ), 72 ( $C_2H_4N_2O$ ), 73 ( $C_2H_7N_3$ ), 88 ( $CN_2O_3$ ), 99 ( $C_3H_5N_3O$ ), 117 ( $C_3H_7N_3O_2$ ), 118 ( $C_2H_6N_4O_2$ ), 119 ( $C_2H_5N_3O_3$ ), 146 ( $C_3H_6N_4O_3$ ), 149 ( $C_4H_{11}N_3O_3$ ), and 191 ( $C_3H_5N_5O_5$ ) in the mass spectrum were detected for the first time in photolysis experiments. Dose-dependent studies in conjunction with wavelength-dependent photolysis experiments aid in identifying key primary and secondary species as well as distinguish pathways that are preferred at higher and lower photon energies. Mechanisms based on previously reported gas-phase and condensed-phase calculations<sup>35–37,41,42,51,52</sup> were exploited to propose the formation pathways of the observed products. Experimental results suggest that N–NO<sub>2</sub> bond fission and nitro–nitrite isomerization are the initial steps in the UV photolysis of RDX. Intriguingly, previously unidentified higher molecular weight products observed at  $m/z = 73, 88, 99, 119, 146, 149,$  and 191 could originate after nitro–nitrite isomerization process. On the basis of our observations, we propose probable reaction pathways that are involved in the photolysis of RDX and recommend further research endeavors in this field.

## 2. METHODS

**2.1. Experimental Section.** The experiments were performed in an ultrahigh vacuum (UHV) surface science chamber evacuated to a base pressure of a few  $10^{-10}$  Torr exploiting magnetically levitated turbo molecular pumps coupled to oil-free dry scroll pumps (Figure S1).<sup>53–55</sup> A highly reflected silver substrate coated with a thin film of RDX at a thickness of  $16.0 \pm 1.0 \mu\text{m}$  is sandwiched to an oxygen free high conductivity copper (OFHC) coldfinger via indium foil. This entire unit is attached to a UHV compatible two-stage

closed-cycle helium refrigerator (Sumitomo Heavy Industries, RDK-415E), which reduces the temperature of the substrate to  $5.0 \pm 0.1$  K. A silicon diode (Lakeshore DT-670) and a cartridge heater are attached to the coldfinger to monitor and control the temperature of the substrate. This assembly is horizontally rotated and vertically translated utilizing a doubly differentially pumped rotary feedthrough (Thermoionics Vacuum Products, RNN-600/FA/MCO) and a UHV compatible bellow (McAllister, BLT106), respectively. After the RDX samples have been cooled to 5 K, infrared spectra of the samples were recorded in the region of 4000 to  $600 \text{ cm}^{-1}$  at a resolution of  $4 \text{ cm}^{-1}$  employing a Fourier-transform infrared spectrometer (FTIR; Nicolet 6700). All FTIR measurements were performed in an absorption–reflection–absorption mode at a reflection angle of  $43^\circ$  to the substrate normal. We determined the thickness of the RDX film through eq 1

$$d = \frac{N}{2\sqrt{n^2 - \sin^2\theta}(\nu_1 - \nu_2)} \quad (1)$$

where  $d$  is the thickness of the film,  $N$  the number of interference fringes observed in the FTIR spectrum due to fringing effect,  $n$  the refractive index of RDX ( $n = 1.49$ ),<sup>56</sup>  $\theta$  the angle of incidence ( $43^\circ$ ), and  $\nu_1$  and  $\nu_2$  the start and end points of the spectrum in  $\text{cm}^{-1}$  covering the fringes. After acquiring the reference IR spectrum of the RDX sample, each film was exposed to the pulsed UV light (radius:  $0.55 \pm 0.05 \text{ cm}$ ) at photon energies lower than the adiabatic ionization energy of RDX (9.99–10.2 eV) and at an angle of  $0^\circ$  relative to the normal of the substrate.<sup>47,48</sup> The chemical changes in the RDX film were monitored online and in situ via an FTIR spectrometer during the photolysis.

To investigate the effect of the excitation wavelength on the photolysis mechanism of RDX, we chose four distinct wavelengths, 254 nm (4.88 eV), 236 nm (5.25 eV), 222 nm (5.58 eV), and 206 nm (6.02 eV). Here, 254, 236, and 222 nm are generated via frequency doubled output of a dye laser pumped by an Nd:YAG laser (30 Hz, 10 ns, 100 mJ pulse<sup>-1</sup>); 206 nm photons are generated via difference frequency mixing of the doubled output and the fundamental of a dye laser pumped by an Nd:YAG laser (30 Hz, 10 ns, 267 mJ pulse<sup>-1</sup>). The RDX samples were exposed to aforementioned UV light over an area of  $0.9 \pm 0.1 \text{ cm}^2$  for 60 min. The irradiation dose ( $D$ ) in units of  $\text{eV molecule}^{-1}$  is calculated at each irradiation wavelength (Table 2) using eqs 2–3.<sup>25</sup>

$$\frac{\text{number of photons}}{\text{molecule}} = \frac{t \times \left(\frac{P}{E_p}\right)}{N} \quad (2)$$

**Table 2.** Parameters Utilized to Calculate the Dose ( $D$ ;  $\text{eV molecule}^{-1}$ ) at the Photolysis Wavelengths of 254 nm (4.88 eV), 236 nm (5.25 eV), 222 nm (5.58 eV), and 206 nm (6.02 eV)

wavelength ( $\lambda$ , nm)	integrated absorption coefficient ( $A_{\text{exp}}$ , $\text{cm molecule}^{-1}$ ) <sup>a</sup>	penetration depth ( $\delta_p$ , $\mu\text{m}$ )	laser intensity ( $P$ , $\text{J s}^{-1} \text{cm}^{-2}$ )	photon energy ( $E_p$ , J)	irradiation time ( $t$ , s)	photons molecule <sup>-1</sup>	dose ( $D$ , $\text{eV molecule}^{-1}$ )
254	$2.3 \times 10^{-15}$	$11.1 \pm 0.7$	$(7.8 \pm 0.5) \times 10^{-3}$	$7.82 \times 10^{-19}$	3600	$8.0 \pm 1.0$	$39.0 \pm 5.0$
236	$5.8 \times 10^{-15}$	$9.4 \pm 0.6$	$(7.8 \pm 0.5) \times 10^{-3}$	$8.42 \times 10^{-19}$	3600	$12.7 \pm 1.3$	$66.8 \pm 7.0$
222	$3.3 \times 10^{-15}$	$9.3 \pm 0.6$	$(7.8 \pm 0.5) \times 10^{-3}$	$8.95 \times 10^{-19}$	3600	$9.1 \pm 1.0$	$50.8 \pm 5.0$
206	$8.4 \times 10^{-15}$	$8.1 \pm 0.5$	$(7.8 \pm 0.5) \times 10^{-3}$	$9.64 \times 10^{-19}$	3600	$13.8 \pm 1.4$	$83.0 \pm 8.0$

<sup>a</sup>Integrated absorption coefficients ( $A_{\text{exp}}$ ) of RDX is derived by integrating the molar absorptivity ( $\epsilon_i$ ;  $\text{L mol}^{-1} \text{cm}^{-1}$ ) vs wavenumber graph acquired from the ref 49.



ReTOF-MS). In the PI-ReTOF-MS setup, we utilized pulsed vacuum ultraviolet (VUV) light at 10.49 eV to softly photoionize the subliming molecules. The ions produced in the photoionization process of the neutrals are then separated in the reflectron time-of-flight tube based on their mass-to-charge ratio and eventually detected via a dual chevron configured microchannel plate (MCP) detector (Jordan TOF Products Inc.). The MCP detector generates the signal, which is amplified via a preamplifier (Ortec 9305) and shaped with a 100 MHz discriminator (Advanced Research Instruments Corporation; F-100TD). A computer-based multichannel scaler receives the signal from the discriminator and records it using 4 ns bin widths triggered at 30 Hz by a pulse delay generator (Quantum Composers 9518). 3600 sweeps are collected per mass spectrum per 1 K increase in the temperature during the TPD phase.

**2.2. Sample Preparation.** RDX samples were procured from BAE Systems, Inc. prepared according to the MIL-DTL-398 D (Military Specification, Detail Specification RDX, 12 DEC 1996); this specifies an HMX (1,3,5,7-tetranitro-1,3,5,7-tetrazoctane;  $C_4H_8N_8O_8$ ) impurity in RDX at levels from 4% to 17%. The maximum permissible quantity of other impurities if present is 0.08%. The impurities were removed from the production grade RDX through recrystallization process in acetone (Fisher Scientific, Inc.). Nuclear magnetic resonance (NMR) spectrum was measured to characterize the recrystallized RDX. The  $^{13}C$  NMR spectra of the crude and recrystallized RDX measured using a Spinsolve 60 Carbon benchtop 60 MHz NMR spectrometer after dissolving in dimethyl sulfoxide- $d_6$  (DMSO- $d_6$ ) solvent are depicted in Figure S3. The peaks associated with the chemical shift of HMX disappears after recrystallization which indicates that RDX has been sufficiently purified to a level of at least 99.9%.<sup>59</sup> Drop-casting method has been utilized to prepare a thin-film of RDX on the silver substrate. For the drop-casting, about 2 mg of recrystallized (purified) RDX is dissolved in 3 g of methyl ethyl ketone (MEK; Acros Organics) inside a vial. Sonication and mild heating at 305 K ensure complete dissolution of the RDX in MEK. Using a glass pipet, a drop of RDX/MEK solution was deposited onto the silver substrate and then left for drying. A uniform layer of RDX is observed after the evaporation of solvent and characterized via infrared spectroscopy.

### 3. RESULTS AND DISCUSSION

**3.1. IR Spectroscopy.** **3.1.1. Qualitative Analysis.** Figures 1 and 2 display infrared (IR) difference spectra of RDX collected at 5 K after exposure to 254 (4.88), 236 (5.25), 222 (5.58), and 206 nm (6.02 eV) light, respectively. Negative “absorptions” manifest a decrease of the intensity of RDX vibrational bands due to photolysis, while infrared features of the products are observed along the positive scale. Prominent vibrational features of the RDX are observed in the spectral regions of 3100–3000  $cm^{-1}$  and 1600–600  $cm^{-1}$ ; which are in excellent agreement with the IR spectrum of RDX reported in the literature (Table 4).<sup>60,61</sup> The amorphous nature of the RDX-film used in the present study is evident from broad and diffuse infrared absorptions measured before the irradiation (Figure S4b). The crystalline phase of RDX-film displays sharp vibrational bands with narrow bandwidth (Figure S4a).<sup>14</sup> The fundamentals of RDX at 3066 and 2989  $cm^{-1}$  are attributed to  $CH_2$  asymmetric and symmetric vibrations, respectively. A broad and intense absorption band centered at 1581  $cm^{-1}$

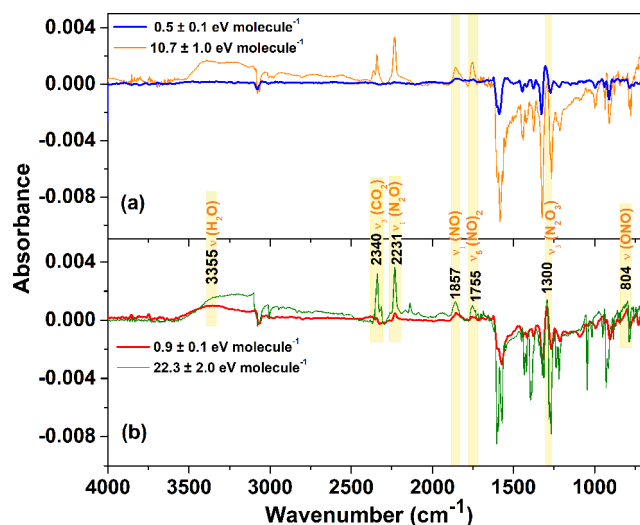


**Figure 2.** Difference infrared spectra of RDX collected at 5K after exposure to (a) 254 nm at doses of  $10.7 \pm 1.0$  and  $0.5 \pm 0.1$  eV molecule $^{-1}$  and (b) 206 nm at doses of  $22.3 \pm 2.0$  eV and  $0.9 \pm 0.02$  eV molecule $^{-1}$ . For clarity, only assignments of the bands corresponding to the products observed at low dose experiments are provided. For the assignments of other bands, please refer to Figure 1.

corresponds to antisymmetric stretching modes of  $-NO_2$  (nitro) group. The characteristic stretching vibration of nitramine bond ( $N-NO_2$ ) appears at 1323  $cm^{-1}$  adjacent to 1267  $cm^{-1}$  band ascribed to symmetric stretching mode of  $-NO_2$  group. The in-plane and out-of-plane bending modes of  $-CH_2$  group are observed at 1442 and 1377  $cm^{-1}$  respectively. The ring vibrations of RDX prevail the spectral regions 1100–1000 and 900–700  $cm^{-1}$ .

After the irradiation new vibrational features appear in the regions 3500–3100, 2340, 2231, 2138, 2079, 1861, and 1756  $cm^{-1}$ , which can be ascribed to photolysis products of RDX (Table 4). A broad absorption feature covering the spectral range from 3500 to 3100  $cm^{-1}$  arises from OH stretching modes of water ( $H_2O$ ) and nitrous acid (HONO).<sup>62–64</sup> Prominent bands at 2340, 2231, 2138, 2079, 1861, and 1756  $cm^{-1}$  are assigned to carbon dioxide ( $CO_2$ ), dinitrogen monoxide ( $N_2O$ ), carbon monoxide (CO), formyl radical (HCO), nitrogen monoxide (NO), and the nitrogen monoxide dimer ( $[NO]_2$ ), respectively.<sup>14,16,65</sup> The observed vibrational features of these products are in excellent agreement with those reported by Alix et al. after photodecomposition of RDX employing a broadband UV light.<sup>16</sup> An absorption feature at 1300  $cm^{-1}$  is also observed (see Figure 2) which can be assigned to  $O-N=O$  symmetric stretching mode of either dinitrogen trioxide ( $N_2O_3$ ) and/or nitrogen dioxide ( $NO_2$ ).<sup>66</sup> However, the symmetric stretch of  $NO_2$  is very weak in intensity; therefore, based on the observed intensity of 1300  $cm^{-1}$  band in our IR spectrum, it could be assigned to  $N_2O_3$ . It is important to mention that dinitrogen trioxide ( $N_2O_3$ ) could either form via a barrier-less radical recombination of nitrogen monoxide (NO) and nitrogen dioxide ( $NO_2$ ) or through bimolecular reaction of nitrous acid (HONO); the latter pathway has a barrier of about 66 kJ mol $^{-1}$ .<sup>67,68</sup> The barrierless radical–radical recombination seems to be favorable since under UV exposure, nitrous acid (HONO) dissociates rapidly to OH and NO radicals.<sup>69,70</sup>

Table 4. (a) Infrared Features of RDX before Irradiation and (b) New Vibrational Bands Appeared after Irradiation at 5 K

(a) Before Irradiation			
wavenumber observed (cm <sup>-1</sup> )	wavenumber literature (cm <sup>-1</sup> ) <sup>61</sup>	assignments	carrier
3066	3068	$\nu^{\text{as}}(\text{CH}_2)$	C–H asymm. stretch
2989	3004	$\nu^{\text{s}}(\text{CH}_2)$	C–H symm. stretch
1581	1576	$\nu^{\text{as}}(\text{NO}_2)$	NO <sub>2</sub> asymm. stretch
1442	1435	$\beta(\text{CH}_2)$	CH <sub>2</sub> bending in plane
1377	1391	$\gamma(\text{CH}_2)$	CH <sub>2</sub> bending out of plane
1323	1322	$\nu^{\text{s}}(\text{N–NO}_2)$	N–N symm. stretch
1267	1275	$\nu^{\text{s}}(\text{NO}_2)$	NO <sub>2</sub> symm. stretch
1218	1219	$\nu(\text{N–C–N})$	ring skeletal vibrations
1083	1040	$\nu^{\text{as}}(\text{ring})$	ring asymm. vibrations
1000	1020	$\nu^{\text{as}}(\text{ring})$	ring asymm. vibrations
910	917	$\gamma(\text{CH}_2)$	CH <sub>2</sub> bending out of plane
779	790	$\nu(\text{C–N–C})$	ring skeletal vibrations
(b) After Irradiation			
wavenumber observed (cm <sup>-1</sup> )	wavenumber literature (cm <sup>-1</sup> ) <sup>61</sup>	assignments	carrier
3500–3100		$\nu(\text{H}_2\text{O})$	O–H stretch of H <sub>2</sub> O
2340	2342 <sup>14</sup>	$\nu_3(\text{CO}_2)$	C=O stretch of CO <sub>2</sub>
2231	2227 <sup>16</sup>	$\nu_1(\text{N}_2\text{O})$	N=N stretch of N <sub>2</sub> O
2138	2140 <sup>16</sup>	$\nu_1(\text{CO})$	C=O stretch of CO
2079	2085	$\nu(\text{HCO})$	C=O stretch of HCO
1861	1864 <sup>14</sup>	$\nu_1(\text{NO})$	N=O stretch of NO
1756	1757 <sup>65</sup>	$\nu_5([\text{NO}]_2)$	N=O stretch of [NO] <sub>2</sub>
1300	1305 <sup>66</sup>	$\nu_3(\text{N}_2\text{O}_3)$	O=N=O stretch of N <sub>2</sub> O <sub>3</sub>
804	812 <sup>71</sup>	$\nu(-\text{ONO})$	N–O stretch of –ONO

It is intriguing to analyze the infrared spectra recorded during the dose-dependent photolysis experiments conducted at irradiation wavelengths of 254 nm (4.88 eV) and 206 nm (6.02 eV). Figure 2a reveals the IR spectra recorded after exposure to 254 nm UV light at a dose of  $10.7 \pm 1.0$  eV molecule<sup>-1</sup> (high dose) and  $0.5 \pm 0.1$  eV molecule<sup>-1</sup> (low dose). At the low dose experiment, only product corresponding to NO (nitrogen monoxide, 1857 cm<sup>-1</sup>), [NO]<sub>2</sub> (nitrogen monoxide dimer, 1755 cm<sup>-1</sup>), and N<sub>2</sub>O<sub>3</sub> (dinitrogen trioxide, 1292 cm<sup>-1</sup>) are prominent.<sup>66</sup> This may imply that these products (NO and N<sub>2</sub>O<sub>3</sub>) rapidly develop during the initial stage of the decomposition relative to alternative products like CO<sub>2</sub>, N<sub>2</sub>O, CO, and H<sub>2</sub>O, which are considered “end members” of the decomposition. The IR spectrum recorded after exposure to 206 nm at a dose of  $0.9 \pm 0.1$  eV molecule<sup>-1</sup> reveals product bands corresponding to nitrogen monoxide (NO), nitrogen monoxide dimer ([NO]<sub>2</sub>), dinitrogen trioxide (N<sub>2</sub>O<sub>3</sub>) along with dinitrogen monoxide (N<sub>2</sub>O) carbon dioxide (CO<sub>2</sub>), and water (H<sub>2</sub>O). A new absorption feature emerges at 804 cm<sup>-1</sup> which can be attributed to stretching mode of the nitrite (-ONO) group.<sup>71</sup> Although the IR spectra investigated after irradiation at 254 and 206 nm are qualitatively similar for both high dose experiments, we observe noticeable difference in low dose studies. Even at a dose of  $0.9 \pm 0.1$  eV molecule<sup>-1</sup>, the exposure to 206 nm results in the formation of CO<sub>2</sub>, N<sub>2</sub>O, and H<sub>2</sub>O, which were not observed at 254 nm at a similar dose; this suggests that the decomposition of RDX is faster at a shorter wavelength, i.e., close to the absorption maximum of RDX. When exposed to the lowest doses of  $0.10 \pm 0.02$  and  $0.20 \pm 0.02$  eV molecule<sup>-1</sup> at 254 and 206 nm, respectively, the absorptions of the new products are not detectable in the IR spectrum; the intensity of the RDX bands decreases by only  $15 \pm 2\%$ .

**3.1.2. Quantitative Analysis: Mass Balance.** To quantify the number of RDX molecules decomposed and the products

formed during the photolysis, we calculated their column densities using a modified Lambert–Beer law equation.<sup>57,72</sup> The integrated absorption coefficients are acquired from the literature as  $5.1 \times 10^{-17}$  cm molecule<sup>-1</sup> for the NO<sub>2</sub> asymmetric stretching mode of RDX at 1581 cm<sup>-1</sup>.<sup>73</sup> The N=O stretch of nitrogen monoxide (NO;  $\nu_1$ ; 1861 cm<sup>-1</sup>) and of the nitrogen monoxide dimer ([NO]<sub>2</sub>;  $\nu_5$ ; 1756 cm<sup>-1</sup>) hold integrated band strengths of  $5.2 \times 10^{-17}$  and  $9.3 \times 10^{-17}$  cm molecule<sup>-1</sup>, respectively.<sup>74</sup> The dinitrogen trioxide (N<sub>2</sub>O<sub>3</sub>) was identified via its O–N=O stretching mode ( $\nu_3$ ; 1300 cm<sup>-1</sup>), which has an integrated absorption coefficient of  $4.6 \times 10^{-17}$  cm molecule<sup>-1</sup>.<sup>74</sup> The column density of N<sub>2</sub>O (dinitrogen monoxide) is measured at 2231 cm<sup>-1</sup> ( $\nu_1$ ; N=N stretching mode) using an integrated band strength of  $5.2 \times 10^{-17}$  cm molecule<sup>-1</sup>.<sup>72</sup> The C=O stretch of carbon dioxide (CO<sub>2</sub>;  $\nu_3$ ; 2340 cm<sup>-1</sup>) and carbon monoxide (CO;  $\nu_1$ ; 2138 cm<sup>-1</sup>) holds integrated band strengths of  $7.6 \times 10^{-17}$  and  $1.1 \times 10^{-17}$  cm molecule<sup>-1</sup> respectively.<sup>75</sup> The broad absorption band in the region 3500–3100 cm<sup>-1</sup> attributed to O–H stretch of water has an averaged absorption coefficient of  $2.0 \times 10^{-16}$  cm molecule<sup>-1</sup>.<sup>75</sup> The integrated area of the vibrational bands of the reactant/products and their corresponding integrated absorption coefficients are utilized to determine the column densities in the photolysis experiments conducted at 254 and 206 nm; these findings are listed in Table S2 of the Supporting Information.

The photolysis at 254 nm at a dose of  $10.7 \pm 1.0$  eV molecule<sup>-1</sup> results in the decomposition of  $(5.6 \pm 0.6) \times 10^{15}$  molecules cm<sup>-2</sup> of RDX, i.e.,  $73 \pm 8\%$ . The amount of NO ( $(1.0 \pm 0.1) \times 10^{15}$  molecules cm<sup>-2</sup>), [NO]<sub>2</sub> ( $(3.1 \pm 0.4) \times 10^{14}$  molecules cm<sup>-2</sup>), N<sub>2</sub>O<sub>3</sub> ( $(3.0 \pm 0.3) \times 10^{14}$  molecules cm<sup>-2</sup>), N<sub>2</sub>O ( $(7.9 \pm 0.8) \times 10^{14}$  molecules cm<sup>-2</sup>), CO<sub>2</sub> ( $(3.9 \pm 0.4) \times 10^{14}$  molecules cm<sup>-2</sup>), CO ( $(5.3 \pm 0.5) \times 10^{14}$  molecules cm<sup>-2</sup>), and

Table 5. Rate Constants Derived by Solving the Reaction Scheme Shown in Figure 4

wavelength ( $\lambda$ , nm)	equation	rate constant	value	units
206	$C_3H_6N_6O_6 \rightarrow 3NO_2 + C_3H_6N_3$	$k_1$	$(1.0 \pm 0.1) \times 10^{-4}$	$s^{-1}$
	$C_3H_6N_6O_6 \rightarrow 3NO + C_3H_6N_3O_3$	$k_2$	$(2.2 \pm 0.2) \times 10^{-5}$	$s^{-1}$
	$C_3H_6N_6O_6 \rightarrow 3NO + 3OH + C_3H_3N_3$	$k_3$	$(3.2 \pm 0.4) \times 10^{-4}$	$s^{-1}$
	$NO_2 + NO \rightarrow N_2O_3$	$k_4$	$(2.0 \pm 0.2) \times 10^{-16}$	$cm^2 \text{ molecule}^{-1} s^{-1}$
	$NO + NO \rightarrow N_2O_2$	$k_5$	$(3.6 \pm 0.4) \times 10^{-18}$	$cm^2 \text{ molecule}^{-1} s^{-1}$
	$C_3H_6N_6O_6 \rightarrow 3N_2O + 3H_2CO$	$k_6$	$(3.1 \pm 0.3) \times 10^{-5}$	$s^{-1}$
	$H_2CO \rightarrow 2H + CO$	$k_7$	$(6.3 \pm 0.6) \times 10^{-1}$	$s^{-1}$
	$OH + H \rightarrow H_2O$	$k_8$	$(2.6 \pm 0.3) \times 10^{-10}$	$cm^2 \text{ molecule}^{-1} s^{-1}$
	$C_3H_6N_6O_6 \rightarrow X$	$k_9$	$(5.1 \pm 0.5) \times 10^{-4}$	$s^{-1}$
254	$C_3H_6N_6O_6 \rightarrow 3NO_2 + C_3H_6N_3$	$k'_1$	$(1.6 \pm 0.2) \times 10^{-4}$	$s^{-1}$
	$C_3H_6N_6O_6 \rightarrow 3NO + C_3H_6N_3O_3$	$k'_2$	$(3.0 \pm 0.3) \times 10^{-4}$	$s^{-1}$
	$NO_2 + NO \rightarrow N_2O_3$	$k'_4$	$(9.9 \pm 1.0) \times 10^{-15}$	$cm^2 \text{ molecule}^{-1} s^{-1}$
	$NO + NO \rightarrow N_2O_2$	$k'_5$	$(5.0 \pm 0.5) \times 10^{-18}$	$cm^2 \text{ molecule}^{-1} s^{-1}$
	$C_3H_6N_6O_6 \rightarrow X$	$k'_9$	$(1.6 \pm 0.2) \times 10^{-3}$	$s^{-1}$

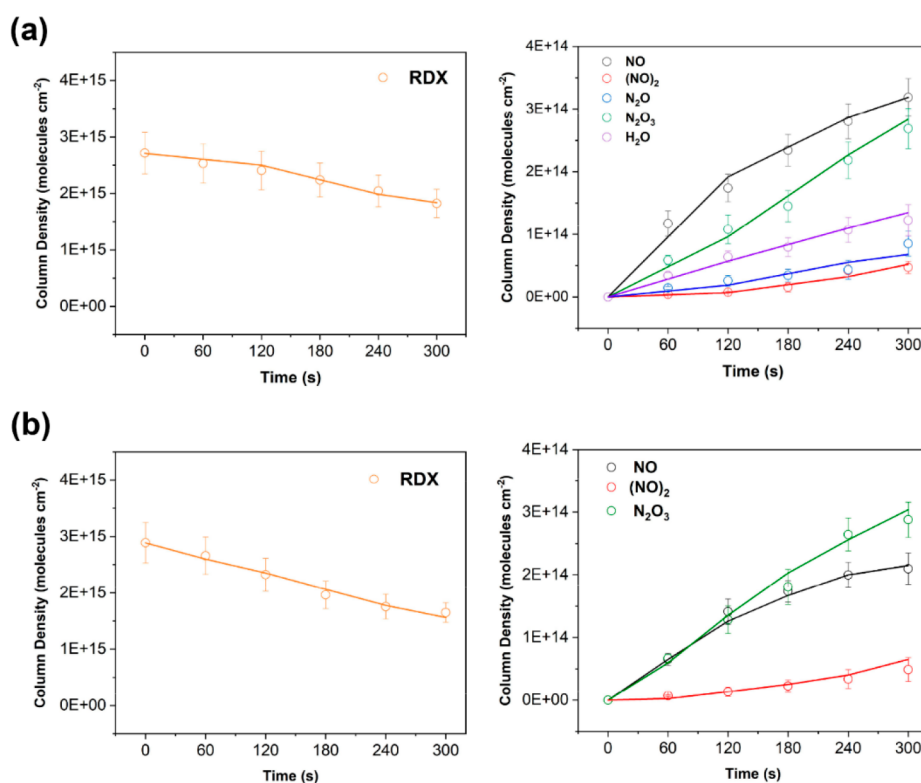


**Figure 3.** Temporal evolution of the column densities of the reactant at  $1581 \text{ cm}^{-1}$  (RDX) and of the products at  $1861 \text{ cm}^{-1}$  (NO),  $1757 \text{ cm}^{-1}$  ( $[NO]_2$ ),  $2227 \text{ cm}^{-1}$  ( $N_2O$ ),  $1305 \text{ cm}^{-1}$  ( $N_2O_3$ ), and  $3500\text{--}3100 \text{ cm}^{-1}$  ( $H_2O$ ) during the photodissociation of RDX at (a) 206 nm at a dose of  $0.9 \pm 0.02 \text{ eV molecule}^{-1}$  and (b) 254 nm at a dose of  $0.5 \pm 0.1 \text{ eV molecule}^{-1}$ . Solid line represents the kinetic fits obtained solving the coupled differential equations leading to the reaction scheme defined in Figure 4 and Table 5.

$H_2O$  ( $(5.8 \pm 0.6) \times 10^{14} \text{ molecules cm}^{-2}$ ) formed during photolysis accounts for  $69 \pm 7\%$  of the decomposed RDX molecules. This implies that 30% of the decomposed molecules could not be identified via infrared spectroscopy; these molecules could belong to higher order products and/or are obscured by the fundamentals of the RDX. In the low dose experiment, the amount of RDX molecules destroyed is  $(1.2 \pm 0.2) \times 10^{15} \text{ molecules cm}^{-2}$ , which is only 43  $\pm$  5% of the initial column density ( $(2.9 \pm 0.2) \times 10^{15} \text{ molecules cm}^{-2}$ ). At this dose, the quantity of the NO ( $(2.1 \pm 0.3) \times 10^{14} \text{ molecules cm}^{-2}$ ),  $[NO]_2$  ( $(2.8 \pm 0.3) \times 10^{13} \text{ molecules cm}^{-2}$ ), and  $N_2O_3$  ( $(2.2 \pm 0.2) \times 10^{14}$

$\text{molecules cm}^{-2}$ ) products formed accounts for only  $36 \pm 3\%$  of the photolyzed RDX molecules. Therefore, we can conclude that almost 74% of the decomposed products were unidentified through IR spectroscopy.

Upon photolysis at 206 nm at a dose of  $22.3 \pm 2.0 \text{ eV molecule}^{-1}$ , about  $(4.5 \pm 0.5) \times 10^{15}$  RDX molecules  $\text{cm}^{-2}$  dissociate; this corresponds to 83  $\pm$  8% of the initial column density ( $(5.4 \pm 0.5) \times 10^{15} \text{ molecules cm}^{-2}$ ). The amount of products such as NO ( $(5.2 \pm 0.7) \times 10^{14} \text{ molecules cm}^{-2}$ ),  $[NO]_2$  ( $(2.2 \pm 0.2) \times 10^{14} \text{ molecules cm}^{-2}$ ),  $N_2O_3$  ( $(5.5 \pm 0.6) \times 10^{14} \text{ molecules cm}^{-2}$ ),  $N_2O$  ( $(1.0 \pm 0.1) \times 10^{15} \text{ molecules cm}^{-2}$ ),  $CO_2$  ( $(6.9 \pm 0.7) \times 10^{14} \text{ molecules cm}^{-2}$ ), CO ( $(5.6 \pm 0.6)$

$\times 10^{14}$  molecules  $\text{cm}^{-2}$ ), and  $\text{H}_2\text{O}$  ( $(4.3 \pm 0.4) \times 10^{14}$  molecules  $\text{cm}^{-2}$ ) formed during photodecomposition accounts for  $87 \pm 8\%$  of the decomposed RDX molecules. It is intriguing to compare the high and low dose photodissociation studies conducted at 206 nm. On the basis of column density calculations, the amount of RDX molecules photolyzed at a dose of  $0.9 \pm 0.1$  eV molecule $^{-1}$  is  $(1.5 \pm 0.2) \times 10^{15}$  molecules  $\text{cm}^{-2}$ , which is only  $55 \pm 5\%$  of the initial number of molecules ( $(2.7 \pm 0.2) \times 10^{15}$  molecules  $\text{cm}^{-2}$ ). Products formed during photodecomposition including NO ( $(3.2 \pm 0.3) \times 10^{14}$  molecules  $\text{cm}^{-2}$ ),  $[\text{NO}]_2$  ( $(7.8 \pm 0.8) \times 10^{13}$  molecules  $\text{cm}^{-2}$ ),  $\text{N}_2\text{O}_3$  ( $(2.6 \pm 0.2) \times 10^{14}$  molecules  $\text{cm}^{-2}$ ),  $\text{N}_2\text{O}$  ( $(7.7 \pm 0.8) \times 10^{13}$  molecules  $\text{cm}^{-2}$ ), and  $\text{H}_2\text{O}$  ( $(1.2 \pm 0.2) \times 10^{14}$  molecules  $\text{cm}^{-2}$ ) accounts for 62% of the decomposed RDX molecules. The comparison of the column densities of the reactant versus products between 254 and 206 nm reveal that the amount of decomposed RDX molecules and that of products formed is higher at later wavelength. These findings are indicative of higher decomposition rates at the shorter wavelength, where  $\pi_{\text{R}} \rightarrow \pi^*$  transitions occur.

**3.1.3. Quantitative Analysis: Kinetic Fitting.** Having identified the species formed during the photolysis of RDX, we are now proposing the underlying mechanism of their formation. This is achieved by exploiting a set of coupled differential equations to numerically fit the temporal profiles of the column densities of the new species formed during the photolysis. A MATLAB script was used to solve the equations and determine the rate constants. Initially assuming first-order and second-order kinetics, the rate constants were optimized to reduce the error between experimentally observed column densities and those predicted from the numerical solutions. The resulting rate constants are listed in Table 5 with the numerical fits plotted in Figure 3 along with the observed column densities. The kinetic scheme is compiled in Figure 4. It is important to mention here that only low dose photolysis

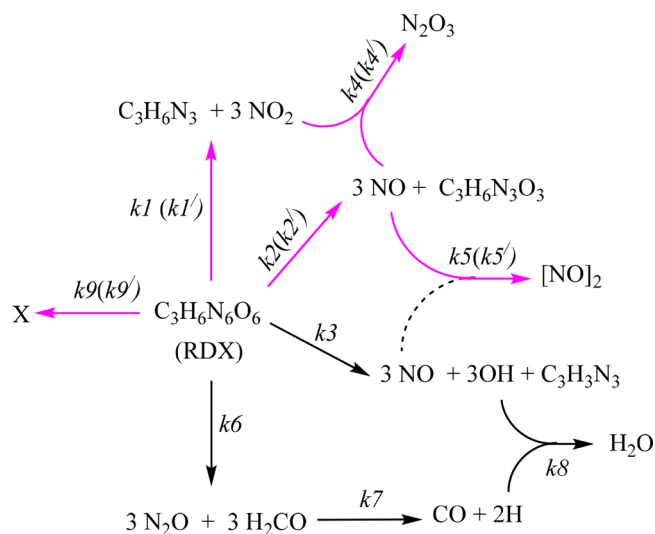


**Figure 4.** Overall reaction scheme utilized for the fit of the temporal profiles of the reactant and products observed via FTIR spectroscopy during photolysis at 254 and 206 nm lights (Figure 2). Pathways of the pink arrows are considered for both 254 and 206 nm photolysis experiments. Rate constants of the reactions corresponding to the 254 nm irradiation are provided in parentheses.

experiments conducted at 206 and 254 nm have been considered here. At high dose, the rate of decomposition may drastically change after some duration because the accumulated products also absorb the UV photons.

As mentioned previously, the FTIR spectrometer detects five products when the sample was exposed to 206 nm light at a dose of  $0.9 \pm 0.1$  eV molecule $^{-1}$ . To rationalize the formation of these products and account for the mass balance, nine key pathways have been considered. First, reaction  $k_1$ , which involves decomposition of RDX into nitrogen dioxide ( $\text{NO}_2$ ) and a higher molecular weight intermediate ( $\text{C}_3\text{H}_6\text{N}_3$ ), has a rate constant of  $(1.0 \pm 0.1) \times 10^{-4}$  s $^{-1}$ . RDX could also decompose to nitrogen monoxide and intermediate  $\text{C}_3\text{H}_6\text{N}_3\text{O}_3$ ; this reaction has a rate constant value of  $(2.2 \pm 0.2) \times 10^{-5}$  s $^{-1}$  ( $k_2$ ). The third decomposition pathway includes elimination of HONO, which could rapidly decompose to nitrogen monoxide (NO) and hydroxy (OH) radicals as mentioned above ( $k_3 = (3.2 \pm 0.4) \times 10^{-4}$  s $^{-1}$ ). The resulting NO and  $\text{NO}_2$  may react to form dinitrogen trioxide ( $\text{N}_2\text{O}_3$ ) molecules ( $k_4 = (2.0 \pm 0.2) \times 10^{-16}$  cm $^2$  molecule $^{-1}$  s $^{-1}$ ). Nitrogen monoxide molecules can undergo self-reaction to form nitrogen monoxide dimer ( $\text{NO}$ ) $_2$ ; this bimolecular reaction has a rate constant of  $k_5 = (3.6 \pm 0.4) \times 10^{-18}$  cm $^2$  molecule $^{-1}$  s $^{-1}$ . It is important to note here that NO molecules formed in the second and third reactions could also combine to form the ( $\text{NO}$ ) $_2$  dimer. RDX could dissociate directly to dinitrogen oxide ( $\text{N}_2\text{O}$ ) and formaldehyde ( $\text{H}_2\text{CO}$ ) ( $k_6 = (3.1 \pm 0.3) \times 10^{-5}$  s $^{-1}$ ). Formaldehyde rapidly decomposes to form carbon monoxide (CO) and atomic/molecular hydrogen ( $k_7 = (6.3 \pm 0.6) \times 10^{-1}$  s $^{-1}$ ). The OH (hydroxy radical) and hydrogen can combine to form water ( $k_8 = (2.6 \pm 0.3) \times 10^{-10}$  cm $^2$  molecule $^{-1}$  s $^{-1}$ ). Finally, a generic reaction involving decomposition of RDX into products which could not be identified through IR spectroscopy has been considered to account for the mass balance as discussed above ( $k_9 = (5.1 \pm 0.5) \times 10^{-4}$  s $^{-1}$ ).

When the RDX samples are exposed to 254 nm light at a low dose ( $0.10 \pm 0.02$  eV molecule $^{-1}$ ), only three products (NO,  $[\text{NO}]_2$ , and  $\text{N}_2\text{O}_3$ ) are detected via IR spectroscopy. Their origin can be justified by four key pathways. (i) stepwise decomposition of RDX leading to three nitrogen dioxide ( $\text{NO}_2$ ) molecules and intermediate  $\text{C}_3\text{H}_6\text{N}_3$  ( $k_1'$ ), (ii) RDX decomposition into nitrogen monoxide (NO) and intermediate  $\text{C}_3\text{H}_6\text{N}_3\text{O}_3$  ( $k_2'$ ), (iii) reaction of  $\text{NO}_2$  and NO molecules to form  $\text{N}_2\text{O}_3$  ( $k_4'$ ), (iv) reaction of two nitrogen monoxide (NO) molecules to form the dinitrogen dioxide ( $\text{NO}$ ) $_2$  ( $k_5'$ ). Finally, a fifth pathway for the decomposition of RDX into products which are unidentified through IR spectroscopy has been considered and expressed generically via the rate constant  $k_9'$ . The aforementioned reaction mechanisms have also been exploited to fit the temporal profiles of the products NO, ( $\text{NO}$ ) $_2$ , and  $\text{N}_2\text{O}_3$  observed in the 206 nm photolysis experiment. Figure 3 further reveals that the profiles of nitrogen monoxide (NO) and dinitrogen monoxide dimer can be fit with fast kinetics, while products such as dinitrogen monoxide ( $\text{N}_2\text{O}$ ) and water ( $\text{H}_2\text{O}$ ) exhibit slower rises. This suggests that the NO and  $\text{N}_2\text{O}_3$  products are likely formed rapidly at the early stage of decomposition. It is important to note here that the total concentration of nitrogen monoxide (NO), i.e., column density of NO + ( $\text{NO}$ ) $_2$  in the reaction medium is always higher than the other products such as dinitrogen oxide ( $\text{N}_2\text{O}$ ), carbon monoxide ( $\text{CO}_2$ ), water

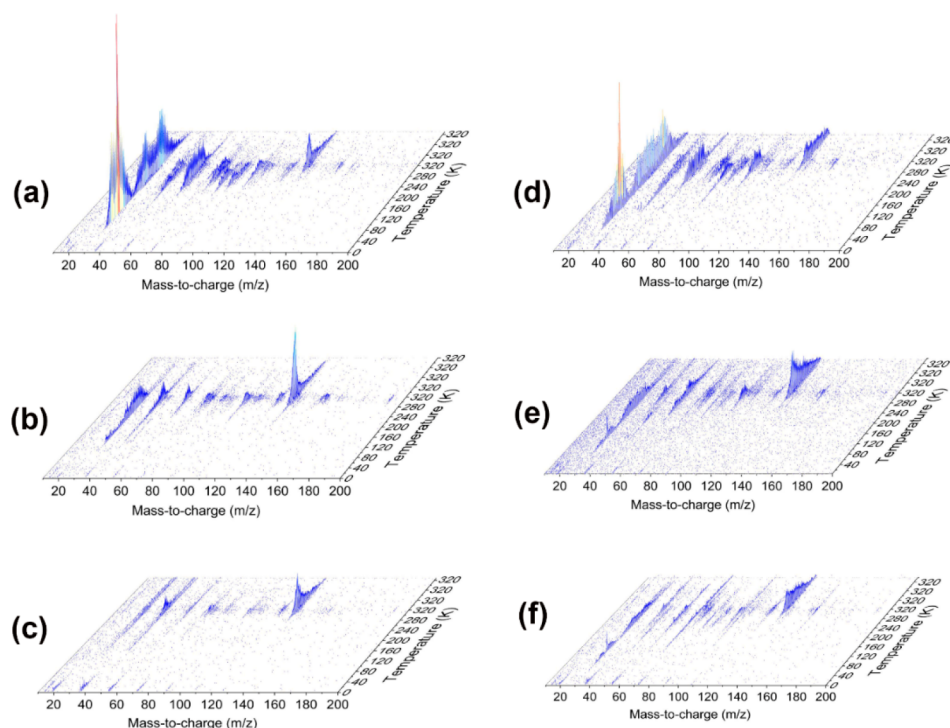


**Figure 5.** Temperature-dependent ReTOF mass spectra collected during the sublimation phase after exposure to 254 nm at doses of (a)  $10.7 \pm 1.0$ , (b)  $0.5 \pm 0.1$ , and (c)  $0.10 \pm 0.02$  eV molecule<sup>-1</sup>. Exposure to 206 nm at doses of (d)  $22.3 \pm 2.0$  eV, (e)  $0.9 \pm 0.02$ , and (f)  $0.20 \pm 0.02$  eV molecule<sup>-1</sup>.

(H<sub>2</sub>O) and dinitrogen trioxide (N<sub>2</sub>O<sub>3</sub>), even at the low dose experiments.

**3.2. Mass Spectrometry.** Single-photon reflectron time-of-flight mass spectrometry enables the detection of wide range of photodecomposition products of RDX based on their mass-to-charge ( $m/z$ ) ratio and sublimation temperature. Parts a–c of Figures 5 reveal the temperature-dependent mass spectra measured after exposing the RDX samples to 254 nm (4.88 eV) at doses of  $10.7 \pm 1.0$ ,  $0.5 \pm 0.1$ , and  $0.10 \pm 0.02$  eV molecule<sup>-1</sup> respectively. Parts d–f Figure 5 show the data after photolysis of RDX at 206 nm (6.02 eV) at doses of  $22.3 \pm 2.0$ ,  $0.90 \pm 0.1$ , and  $0.20 \pm 0.02$  eV molecule<sup>-1</sup>. It is apparent from Figure 5 that the ion counts corresponding to lower molecular weight species are enhanced at the high dose experiment compared to low dose study; higher molecular weight products are more prominent at lower doses. This suggests that higher mass (primary) products eventually decompose to lower weight species as the dose increases. Overall, we observed products holding  $m/z$  values of 30, 31, 42, 44, 45, 46, 57, 58, 59, 60, 71, 72, 73, 74, 75, 81, 87, 88, 89, 97, 98, 99, 101, 105, 117, 118, 119, 128, 130, 146, 149, and 191. The assigned molecular formulas and potential structures of all these products are revealed in Table 6 and Figure 6.

It is intriguing to note here that when RDX samples are exposed to very high doses of  $39.0 \pm 5.0$ ,  $66.8 \pm 7.0$ ,  $50.8 \pm 5.0$ , and  $83.0 \pm 8.0$  eV molecule<sup>-1</sup> at 254, 236, 222, and 206 nm respectively, products corresponding to  $m/z$  values of 57, 60, 87, 98, 105, 117, 118, 119, 130, 146, 149, and 191 are not observed. This proposed that these species, especially higher molecular weight products holding  $m/z = 130$ , 146, 149, and 191, could decompose to any lower molecular weight products upon further photolysis. The mass spectra and the TPD profiles of the individual masses recorded in these experiments are depicted in Figures 7 and 8 respectively. It is essential to

mention here that the ReTOF mass spectrum collected in a blank experiment—that is an experiment conducted without exposing the RDX sample to UV light—did not reveal any signal (Figure S5). This ensures that the product signals observed in the photolysis experiments are solely due to the action of UV photons.

Figure 9 display the TPD traces of the photoproducts of RDX observed after exposure to 254 nm at a dose of  $10.7 \pm 1.0$ ,  $0.5 \pm 0.1$ , and  $0.10 \pm 0.02$  eV molecule<sup>-1</sup>. Signal at  $m/z = 30$  and  $m/z = 31$  can be allocated to nitrogen monoxide (NO; IE = 9.26 eV) and methylamine (CH<sub>3</sub>NH<sub>2</sub>; IE = 8.90 eV), respectively. The maximum intensity at  $m/z = 31$  at 260 K correlates with the second sublimation event of  $m/z = 30$  at 260 K, proposing that at least some of the ion counts recorded at  $m/z = 30$  at 260 K could be due to the fragment of CH<sub>3</sub>NH<sub>2</sub><sup>+</sup>, i.e., CH<sub>3</sub>NH<sup>+</sup>. The appearance energy (AE) of 10.18 eV for CH<sub>3</sub>NH<sup>+</sup> from CH<sub>3</sub>NH<sub>2</sub><sup>+</sup> has been reported by Losing et al., which further corroborates our assignment.<sup>76</sup> In previous experimental studies, ion signal at  $m/z = 30$  has been assigned to formaldehyde (H<sub>2</sub>CO) based on electron impact ionization.<sup>8</sup> In the present study, the photoionization energy of 10.49 eV is lower than the ionization energy of formaldehyde (H<sub>2</sub>CO, IE = 10.88 eV); therefore, the signal at  $m/z = 30$  has to be assigned to nitrogen monoxide (NO; IE = 9.26 eV). Product signal at  $m/z = 42$  has been observed in several studies investigating the decomposition of RDX. Although,  $m/z = 42$  is assigned to diazomethane (H<sub>2</sub>CNN; IE = 8.99 eV) in most of the studies,<sup>10,23,26</sup> our recent investigation on RDX decomposition exploiting isomer selective soft-photoionization technique enabled us to assign it to ketene (H<sub>2</sub>CCO; IE = 9.62 eV).<sup>44</sup> The ion signal at  $m/z = 44$  can be ascribed to dinitrogen monoxide (N<sub>2</sub>O; IE = 12.89 eV) and/or methane diazene holding the molecular formula CH<sub>4</sub>N<sub>2</sub> (IE = 8.81 eV). The photoionization energy of 10.49 eV used in this experiment is

Table 6. Probable Molecular Formulas of the Masses Observed in the ReTOF Mass Spectrometer after Photodecomposition of RDX at 254 and 206 nm<sup>a</sup>

m/z	Molecular formula	254 nm			206 nm			Reference
		High	Low	Lowest	High	Low	Lowest	
30	NO	+	+	+	+	+	+	8
31	CH <sub>3</sub> N	+	-	-	+	+	-	
42	CH <sub>2</sub> N <sub>2</sub>	+	+	+	+	+	+	10, 23
	C <sub>2</sub> H <sub>2</sub> O							44
44	N <sub>2</sub> O	+	-	-	+	-	-	8
	CH <sub>4</sub> N <sub>2</sub>							
45	CH <sub>3</sub> NO	+	+	-	+	-	-	8, 9
46	NO <sub>2</sub>	+	-	-	+	+	-	9
57	C <sub>2</sub> H <sub>3</sub> NO	-	-	-	+	+	+	67
58	C <sub>2</sub> H <sub>6</sub> N <sub>2</sub>	+	+	+	+	+	-	
	CH <sub>2</sub> N <sub>2</sub> O							67, 78
59	C <sub>2</sub> H <sub>5</sub> NO	+	-	-	+	+	-	9
60	N <sub>2</sub> O <sub>2</sub>	+	-	-	-	-	-	79
	C <sub>2</sub> H <sub>8</sub> N <sub>2</sub>							
71	C <sub>2</sub> H <sub>5</sub> N <sub>3</sub>	+	+	+	+	+	+	
72	C <sub>2</sub> H <sub>4</sub> N <sub>2</sub> O	+	+	+	-	-	-	80
73	C <sub>2</sub> H <sub>7</sub> N <sub>3</sub>	+	+	+	+	+	+	
74	CH <sub>2</sub> N <sub>2</sub> O <sub>2</sub>	+	+	+	+	+	+	78, 80
75	C <sub>2</sub> H <sub>5</sub> NO <sub>2</sub>	+	+	+	+	+	+	21
	C <sub>2</sub> H <sub>9</sub> N <sub>3</sub>							
81	C <sub>3</sub> H <sub>3</sub> N <sub>3</sub>	+	+	+	-	-	-	8, 80
87	C <sub>3</sub> H <sub>9</sub> N <sub>3</sub>	+	+	-	+	+	+	
88	CN <sub>2</sub> O <sub>3</sub>	+	+	-	-	-	-	78
	C <sub>2</sub> H <sub>4</sub> N <sub>2</sub> O <sub>2</sub>							78
89	CH <sub>3</sub> N <sub>3</sub> O <sub>2</sub>	+	+	-	-	-	-	
97	C <sub>3</sub> H <sub>3</sub> N <sub>3</sub> O	+	+	+	+	+	+	9
98	C <sub>2</sub> H <sub>2</sub> N <sub>4</sub> O	+	+	+	-	-	-	
99	C <sub>3</sub> H <sub>5</sub> N <sub>3</sub> O	+	+	+	-	-	-	
101	C <sub>2</sub> H <sub>3</sub> N <sub>3</sub> O <sub>2</sub>	+	+	+	+	+	+	80
105	C <sub>2</sub> H <sub>7</sub> N <sub>3</sub> O <sub>2</sub>	+	+	+	-	-	-	
117	C <sub>3</sub> H <sub>7</sub> N <sub>3</sub> O <sub>2</sub>	+	+	+	+	+	+	
118	C <sub>2</sub> H <sub>6</sub> N <sub>4</sub> O <sub>2</sub>	+	+	+	+	+	+	
119	C <sub>2</sub> H <sub>5</sub> N <sub>3</sub> O <sub>3</sub>	+	+	+	+	+	+	
128	C <sub>3</sub> H <sub>4</sub> N <sub>4</sub> O <sub>2</sub>	+	+	+	+	+	+	15, 12
130	C <sub>3</sub> H <sub>6</sub> N <sub>4</sub> O <sub>2</sub>	-	-	-	+	+	+	35, 80
146	C <sub>3</sub> H <sub>6</sub> N <sub>4</sub> O <sub>3</sub>	+	+	+	+	+	+	80
149	C <sub>4</sub> H <sub>11</sub> N <sub>3</sub> O <sub>3</sub>	+	+	+	-	-	-	
191	C <sub>3</sub> H <sub>5</sub> N <sub>5</sub> O <sub>5</sub>	+	+	+	+	+	+	80

<sup>a</sup>High, low and lowest denotes the dose strength. Presence and absence of a signal at a given  $m/z$  value is represented by (+) and (-) signs respectively. Ion signal intensities of the  $m/z$  values marked with blue color are enhanced at a high dose while that of marked with red color are enhanced at a low dose.

lower than the ionization energy of dinitrogen monoxide (N<sub>2</sub>O); therefore, the signal at  $m/z = 44$  should be due to CH<sub>3</sub>NNH (methane diazene). A broad signal at  $m/z = 45$  can be associated with the structural isomers of molecular formula CH<sub>3</sub>NO: nitrosomethane (CH<sub>3</sub>NO; IE = 9.30 eV), formamide (HCONH<sub>2</sub>; IE = 10.16 eV), and formaldehyde oxime (H<sub>2</sub>CNOH; IE = 10.11 eV). Behrens et al. also observed a

product signal at  $m/z = 45$ , which was assigned to molecular formula CH<sub>3</sub>NO based on isotopic scrambling experiment.<sup>8,9</sup> The peak maxima of the TPD profile measured at  $m/z = 45$  at 256 and 316 K correlates with the second and third sublimation events recorded at  $m/z = 30$  implying that the NO<sup>+</sup> fragment of CH<sub>3</sub>NO<sup>+</sup> (nitrosomethane) could contribute to some of the ion counts at  $m/z = 30$  at 256 and 316 K.

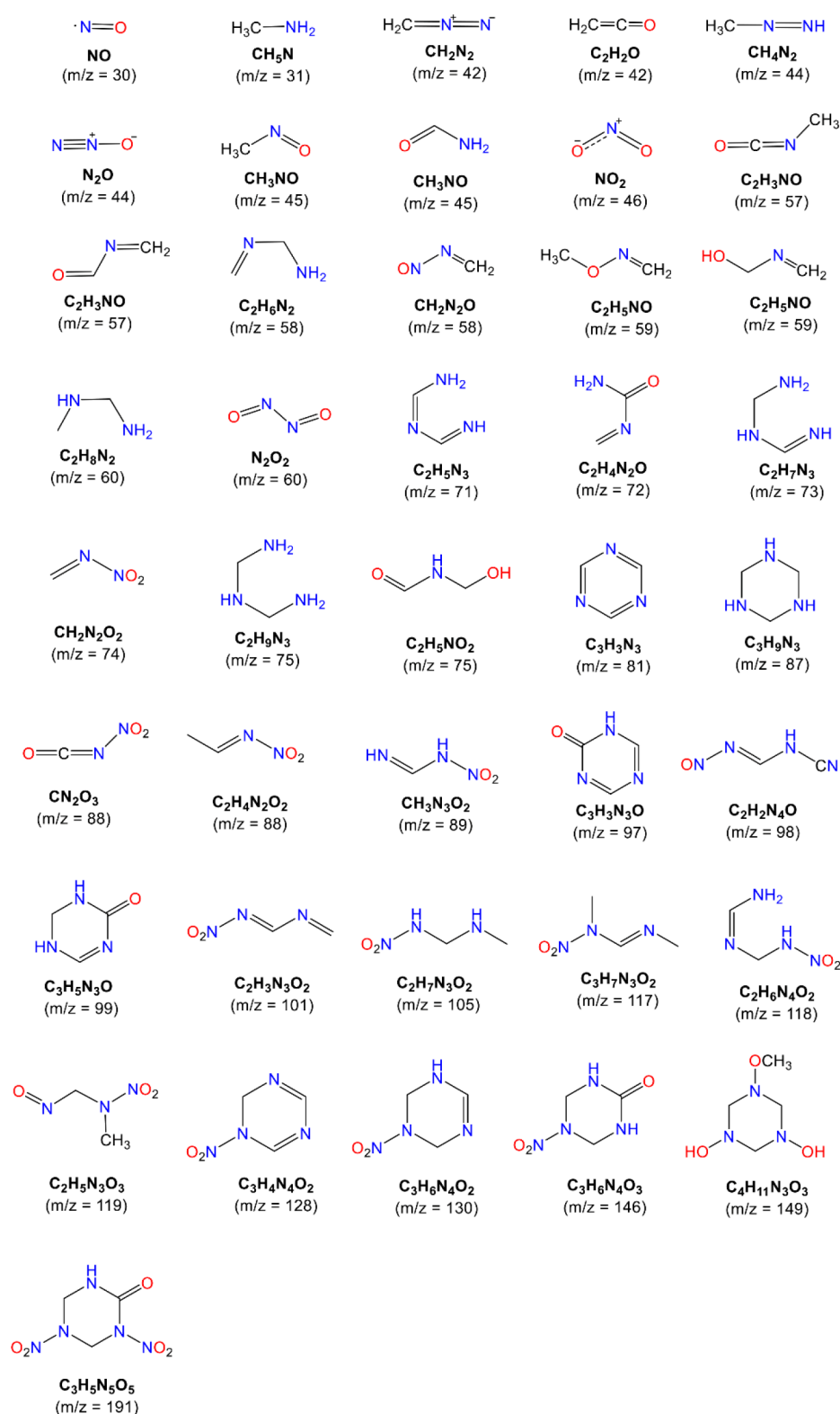


**Figure 6.** Probable structures and molecular formulas of the masses observed in ReTOF mass spectrometer.

Therefore, we can propose that at least a fraction of the ion counts measured at  $m/z = 45$  and  $m/z = 30$  at around 256 and 316 K could be due to  $\text{CH}_3\text{NO}^+$  and its fragment ions  $\text{NO}^+$ , respectively. Dose-dependent experiments show a significant decrease in the ion intensity at  $m/z = 30$  and  $m/z = 45$  at low dose. Signal at  $m/z = 31$  and 44 also disappears in low dose experiments, indicating that these products must be originating

from higher molecular weight products at later stage of the photolysis process. On the other hand, ion counts at  $m/z = 42$  are enhanced in low dose experiments ( $0.5 \pm 0.1$  and  $0.10 \pm 0.02$  eV molecule<sup>-1</sup>) revealing that this product could form at an early stage of decomposition.

The TPD profile recorded at  $m/z = 46$  can be allocated to nitrogen dioxide ( $\text{NO}_2$ ; IE = 9.58 eV).<sup>9</sup> Furthermore, the

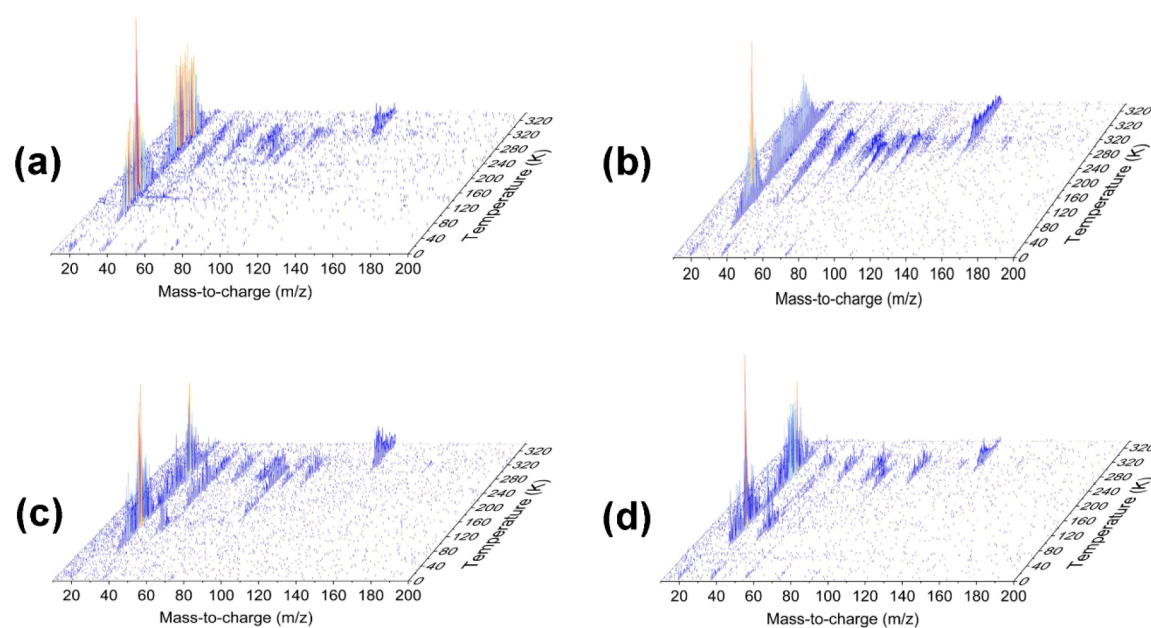


**Figure 7.** Temperature-dependent ReTOF mass spectra collected during the sublimation phase measured after exposure to (a) 254, (b) 236, (c) 222, and (d) 206 nm at doses of  $39.0 \pm 5.0$ ,  $66.8 \pm 7.0$ ,  $50.8 \pm 5.0$ , and  $83.0 \pm 8.0$  eV molecule<sup>-1</sup> respectively.

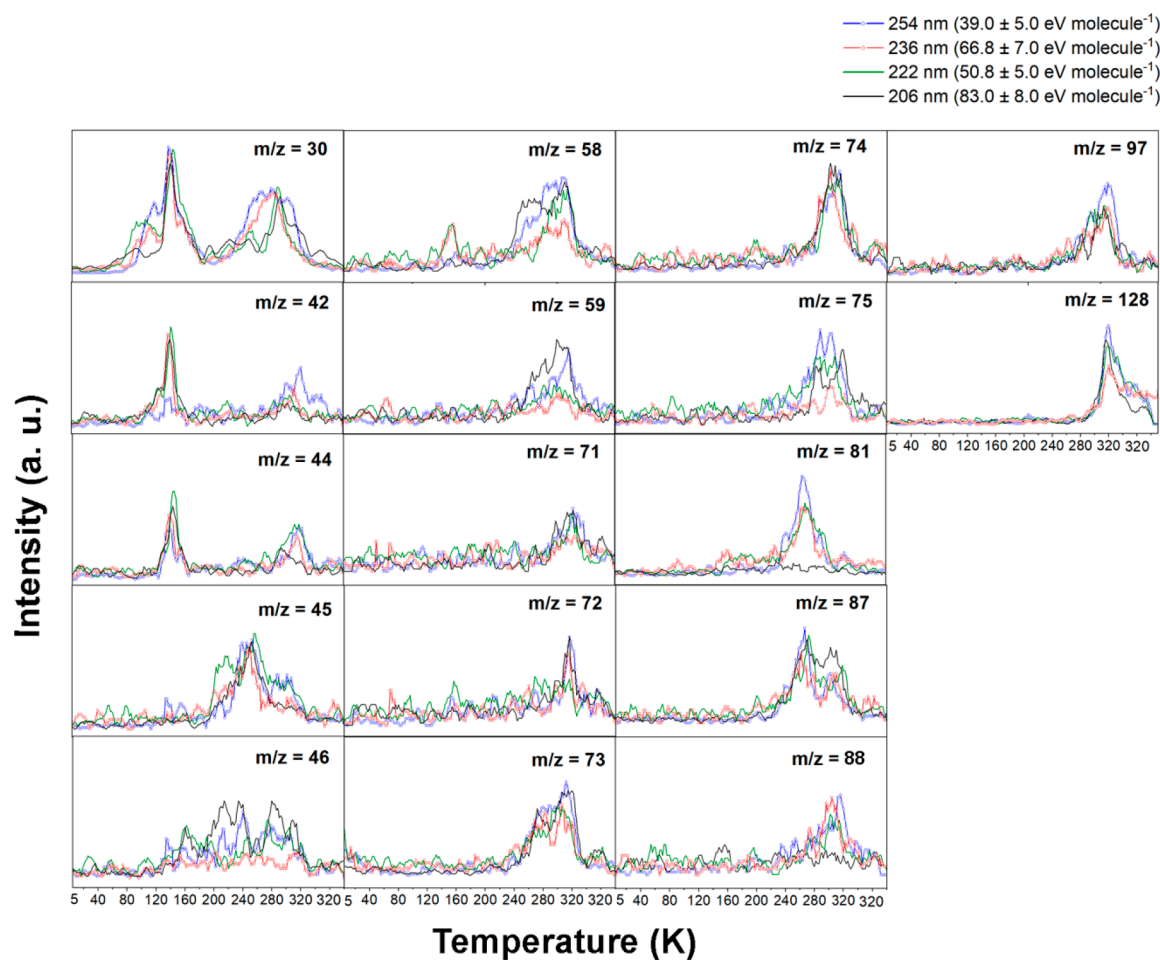


**Figure 8.** TPD profiles of the ion counts recorded at mass-to-charge ratios of 30, 42, 44, 45, 46, 58, 59, 71, 72, 73, 74, 75, 81, 87, 88, 97, and 128 at a photoionization energy of 10.49 eV, after exposure to 254, 236, 222, and 206 nm photons at doses of  $39.0 \pm 5.0$ ,  $66.8 \pm 7.0$ ,  $50.8 \pm 5.0$ , and  $83.0 \pm 8.0$  eV molecule<sup>-1</sup> respectively.

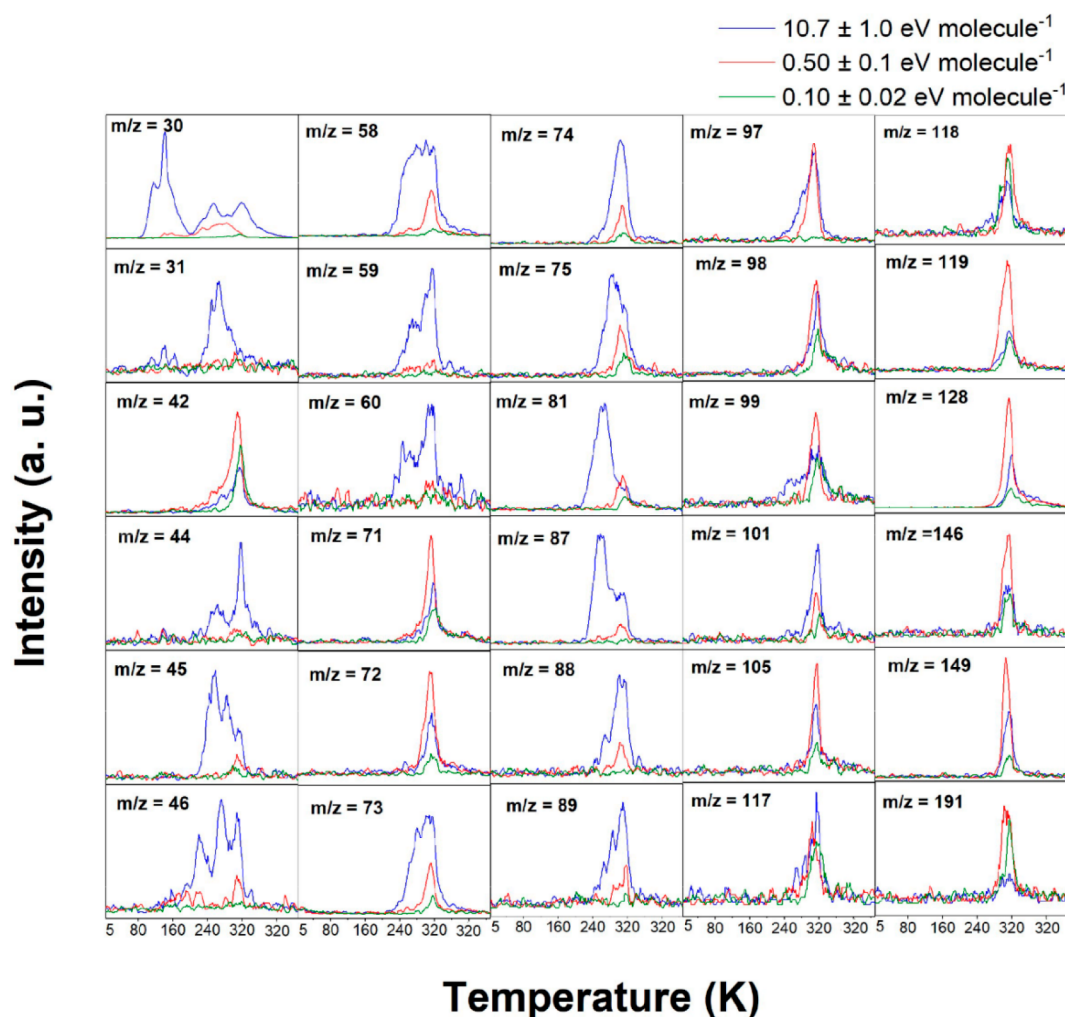


**Figure 9.** TPD profiles of the ion counts recorded at mass-to-charge ratios of 30, 31, 42, 44, 45, 46, 58, 59, 60, 71, 72, 73, 74, 75, 81, 87, 88, 89, 97, 98, 99, 101, 105, 117, 118, 119, 128, 146, 149, and 191 at a photoionization energy of 10.49 eV, after exposure to 254 nm at doses of  $10.7 \pm 1.0$ ,  $0.5 \pm 0.1$ , and  $0.10 \pm 0.02$  eV molecule<sup>-1</sup>.

sublimation events measured at  $m/z = 46$  at around 284 and 316 K correlate with two peaks observed at  $m/z = 30$  at around 284 and 316 K, signifying that fragments of  $\text{NO}_2$ , i.e.,  $\text{NO}^+$ , may contribute to the ion counts measured at  $m/z = 30$  at these temperatures.<sup>77</sup> The signal at  $m/z = 58$  can be assigned to an amine with the molecular formula  $\text{C}_2\text{H}_6\text{N}_2$  or to a nitroso derivative of methylene nitramine ( $\text{CH}_2\text{N}_2\text{O}$ ). In several experimental and computational studies, the product at  $m/z = 58$  has been assigned to  $\text{CH}_2\text{N}_2\text{O}$ .<sup>67,78</sup> The ion signal at  $m/z = 59$  can be attributed to a molecular formula  $\text{C}_2\text{H}_5\text{NO}$  based on previous assignments reported by Behrens and co-workers.<sup>9</sup> The product corresponding to  $m/z = 60$  can be allocated to  $\text{N}_2\text{O}_2$ <sup>79</sup> or designated as the hydrogenated form of the amine moiety allocated to  $m/z = 58$  and hence might be linked to the molecular formula  $\text{C}_2\text{H}_8\text{N}_2$  (*N*-methylmethanediamine). The former ( $\text{N}_2\text{O}_2$ ; 60 amu) could form via self-reaction of nitrogen monoxide (NO). The TPD profiles measured at  $m/z = 59$  and 60 are very similar suggesting that some of the ion counts at  $m/z = 59$  could be due to  $\text{C}_2\text{H}_7\text{N}_2^+$  generated via fragmentation of internally “hot”  $\text{C}_2\text{H}_8\text{N}_2^+$  (*N*-methylmethanediamine;  $m/z = 60$ ) ions. Although the appearance energy (AE) for  $\text{C}_2\text{H}_7\text{N}_2^+$  from  $\text{C}_2\text{H}_8\text{N}_2^+$  (*N*-methylmethanediamine ion) is not known, the AE of fragment  $\text{C}_2\text{H}_7\text{N}_2^+$  from ethylenediamine ( $\text{C}_2\text{H}_8\text{N}_2^+$ ) ion at a photoionization

energy of 9.20 eV has been reported. Therefore, fragmentation of  $\text{C}_2\text{H}_8\text{N}_2^+$  (*N*-methylmethanediamine ion) into  $\text{C}_2\text{H}_7\text{N}_2^+$  at a photoionization energy of 10.49 eV is likely. The ion counts at  $m/z = 46$  and  $m/z = 58$  are reduced by a factor of 2 at low dose ( $0.5 \pm 0.1$  eV molecule<sup>-1</sup>) and show almost negligible counts at the lowest dose ( $0.10 \pm 0.02$  eV molecule<sup>-1</sup>). Similarly, no signal is observed at  $m/z = 59$  and 60 in low dose experiments. These findings provide evidence that species corresponding to  $m/z = 46$ , 58, 59, and 60 could be defined as secondary products. Ions recorded at  $m/z = 71$  are likely linked to an amine holding the molecular formula  $\text{C}_2\text{H}_5\text{N}_3$ . Ions at  $m/z = 72$  can be linked to 1-methylethylamine with the molecular formula  $\text{C}_2\text{H}_4\text{N}_2\text{O}$ . The signal at  $m/z = 72$  has also been observed in electron impact fragmentation of RDX by Yinon et al.<sup>80</sup> Product at  $m/z = 73$  is likely linked to  $\text{C}_2\text{H}_7\text{N}_3^+$  which is hydrogenated counterpart of  $\text{C}_2\text{H}_5\text{N}_3^+$  ( $m/z = 71$ ). The TPD traces measured at these channels ( $m/z = 71, 72$ ) show peak maxima at same temperatures of 310 K. This could be either due to cosublimation of the products or photofragmentation of one species into another. Fragmentation of  $\text{C}_2\text{H}_4\text{N}_2\text{O}^+$  to  $\text{C}_2\text{H}_3\text{N}_2\text{O}^+$  is viable. The TPD profile measured at  $m/z = 74$  can be certainly associated with the monomeric unit of RDX i.e. methylene nitramine ( $\text{H}_2\text{CNNO}_2$ ), based on assignments reported by previous studies.<sup>78,80,81</sup> Ion signal at  $m/z = 75$  can

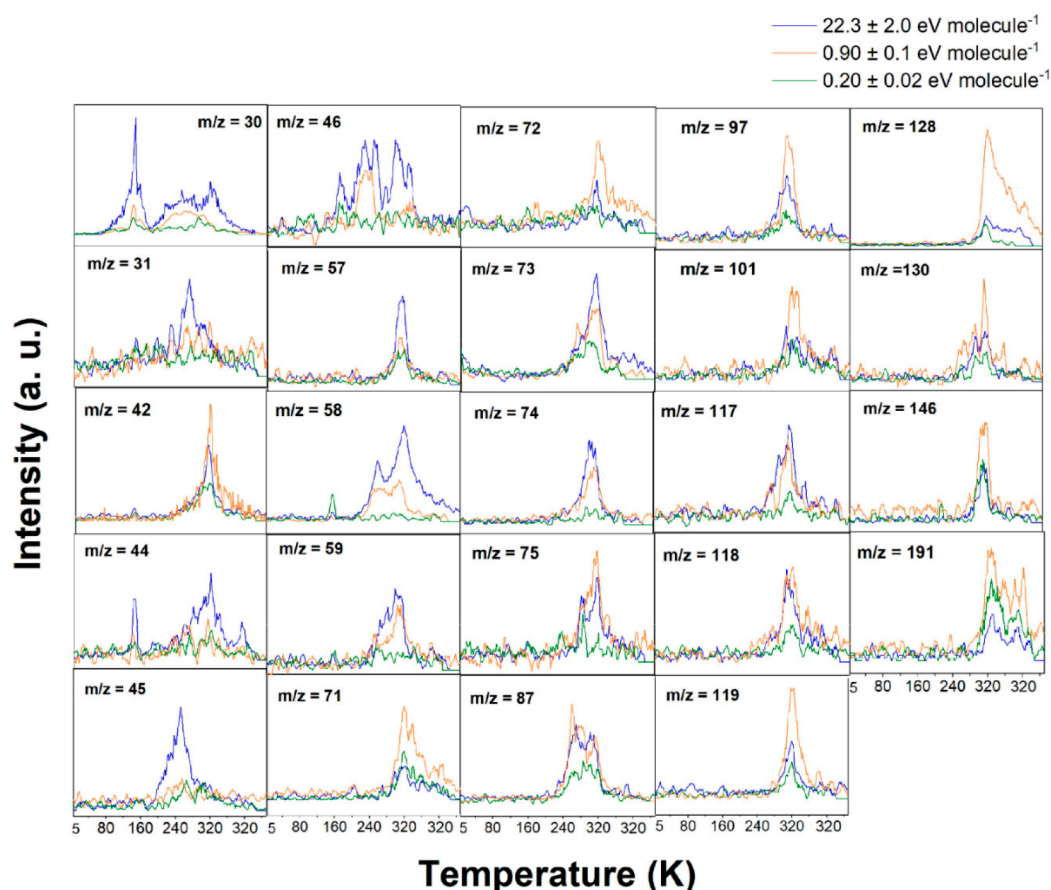


**Figure 10.** TPD profiles of the ion counts recorded at mass-to-charge ratio of 30, 31, 42, 44, 45, 46, 57, 58, 59, 71, 72, 73, 74, 75, 87, 97, 101, 117, 118, 119, 128, 130, 146, and 191 at a photoionization energy of 10.49 eV, after exposure to 206 nm at doses of  $22.3 \pm 2.0$ ,  $0.90 \pm 0.1$ , and  $0.20 \pm 0.02$  eV molecule<sup>-1</sup>.

be allocated to an amine  $C_2H_9N_3$  or *c*-hydroxyl-*N*-methyl formamide ( $C_2H_5NO_2$ ). The latter ( $C_2H_5NO_2^+$ ;  $m/z = 75$ ) has been observed in the thermal decomposition of RDX.<sup>21</sup> Ion counts for species at  $m/z = 71$  and  $72$  increase at a dose of  $0.5 \pm 0.1$  eV molecule<sup>-1</sup>, suggesting that these species could be generated at the early stage of decomposition. On the other hand, intensity of ions signals at  $m/z = 74$  and  $75$  are reduced by a factor of 2 at medium dose and by a factor of 5 at the lowest dose ( $0.10 \pm 0.02$  eV molecule<sup>-1</sup>) providing evidence that products corresponding to  $m/z$  values of 74 and 75 should be originating at a later stage of the photolysis.

TPD traces observed via their ion counts at  $m/z = 81$  and  $87$  can be attributed to species carrying ring moieties of RDX.  $m/z = 81$  has been often associated with triazine ( $C_3H_3N_3$ ; IE = 9.80 eV)<sup>8,80</sup> while  $m/z = 87$  is likely associated as a fully hydrogenated counterpart of 1,3,5-triazine, i.e., 1,3,5-triazinane ( $C_3H_9N_3$ ). Although  $m/z = 81$  has been observed in several experiments,<sup>8,26</sup> there is only a single report of product at  $m/z = 87$ .<sup>15</sup> Signal at  $m/z = 88$  can be ascribed to mononitro compound with the molecular formulas  $CN_2O_3$  or  $C_2H_4N_2O_2$  following the assignments reported by Schroeder.<sup>78</sup> Signal at  $m/z$  values of 89 and 97 can be linked to aminomethyl nitramine ( $CH_3N_3O_2$ ) and oxy-*sym*-triazine (OST;  $C_3H_3N_3O$ ), respectively. The later ( $m/z = 97$ ) has been observed in thermal decomposition studies and was assigned to  $C_3H_3N_3O$ .<sup>9</sup> Products observed at  $m/z = 81$ , 87, 88, and 89 are generated during the later stages of the photodissociation based on the fact that ion counts of these species are reduced

by a factor of 2–3 at low dose ( $0.5 \pm 0.1$  eV molecule<sup>-1</sup>); nearly no counts are observed at the dose of  $0.10 \pm 0.02$  eV molecule<sup>-1</sup>. It is crucial to mention here that fragmented ions of  $CH_3N_3O_2^+$  ( $m/z = 89$ ), i.e.,  $CH_2N_3O_2^+$  and  $CHN_3O_2^+$ , could contribute to some of the ion counts at  $m/z = 88$  and  $87$  respectively; this is evident as the peak maxima of the TPD profile recorded at  $m/z = 89$  is in agreement with the sublimation peak observed at  $m/z = 88$  and  $87$  at around 310 K.

The signal at  $m/z = 98$  is allocated to a mononitroso compound holding the molecular formula  $C_2H_2N_4O$ . Mononitroso species have been proposed to form during RDX decomposition in previous experimental studies.<sup>15,8</sup> The TPD profile recorded at  $m/z = 99$  can be associated with the hydrogenated form of oxy-*sym*-triazine ( $C_3H_3N_3O$ ;  $m/z = 97$ ), hence assigned to the molecular formula  $C_3H_5N_3O$ . Although,  $m/z = 97$  has been observed in previous condensed phase studies investigating the decomposition of RDX, the signature of  $m/z = 99$  has not been observed before. It is also important to note that the maximum of the TPD profile at  $m/z = 99$  corresponds to the data recorded at  $m/z = 98$  and  $97$ ; this suggests that  $C_3H_5N_3O^+$  ( $m/z = 99$ ) could fragment into  $C_3H_4N_3O^+$  and  $C_3H_3N_3O^+$ . Signals at  $m/z = 101$ , 105, 117, and 118 may be allocated to mononitro species holding molecular formulas  $C_2H_3N_3O_2$ ,  $C_2H_7N_3O_2$ ,  $C_3H_7N_3O_2$ , and  $C_2H_6N_4O_2$  respectively. Product at  $m/z = 101$  has been reported by Yinon et al. investigating the fragmentation of RDX and was assigned to  $C_2H_3N_3O_2^+$ .<sup>80</sup> Following similar





$C_2H_5N_3O_3$ . Products holding nitro and nitroso groups have been proposed to form during decomposition of RDX.<sup>8,15</sup> The signal at  $m/z = 128$  can be allotted to the cyclic mononitro moiety ( $C_3H_4N_4O_2$ ). Evidence of  $m/z = 128$  has been reported in previous studies.<sup>15,12</sup> The TPD profile measured at  $m/z = 146$  can be considered as the mononitro counterpart of oxy-sym-triazine, i.e., 5-nitro-1,3,5-triazinan-2-one; therefore, it might be assigned to molecular formula  $C_3H_6N_4O_3$ . Similarly,  $m/z = 191$  can be linked to dinitro form of OST ( $C_3H_3N_5O$ ;  $m/z = 97$ ) holding molecular formula  $C_3H_5N_5O_5$ . The proposed molecular formulas of  $m/z = 146$  and 191 are in agreement with Yinon et al.<sup>80</sup> Although species at  $m/z$  values of 146 and 191 have been observed before in electron fragmentation study of RDX, these species have not been reported previously in UV photolysis experiments. Ion signal at  $m/z = 149$  can be allocated to molecular formula  $C_4H_{11}N_3O_3$ . To the best of our knowledge, signal corresponding to product mass 149 amu have not been observed in previous experiments. Dose-dependent studies reveal that ion intensities of products at  $m/z = 99, 105, 119, 128, 146, 149,$  and 191 are enhanced by a factor of 2 at low dose ( $0.5 \pm 0.1$  eV molecule<sup>-1</sup>) implying that these species are likely formed during the initial stage of the RDX decomposition. These products ( $m/z = 119, 146, 149,$  and 191) have not been identified previously in photolysis experiments.

Figure 10 depicts the TPD profiles of all the individual masses that appeared in the ReTOF-MS after photodecomposition of RDX samples via 206 nm light at a dose of  $22.3 \pm 2.0, 0.90 \pm 0.1,$  and  $0.20 \pm 0.02$  eV molecule<sup>-1</sup>. Products are observed at  $m/z$  values of 30, 31, 42, 44, 45, 46, 58, 59, 71, 72, 73, 74, 75, 87, 97, 101, 117, 118, 119, 128, 146, and 191. These products have been observed during photolysis of RDX at 254 nm and their assignments have been discussed earlier. Although photodecomposition at 206 nm did not generate products corresponding to  $m/z$  values of 60, 81, 89, 98, 99, 105, and 149, we observed few new species at  $m/z = 57$  and 130. The later mentioned species were not identified during RDX photolysis at longer wavelength (254 nm) proposing that at higher photon energy (206 nm) few of the products further dissociates to form new molecular species. Ion signal at  $m/z = 57$  can be assigned to molecular formula  $C_2H_3NO$ . Formation of product corresponding to molecular formula  $C_2H_3NO$  has been supported through computational study. TPD profile collected via  $m/z = 130$  can be linked to the dinitro cyclic moiety with the molecular formula  $C_3H_6N_4O_2$ , based on assignments reported in previous experimental and computational studies.<sup>35,80</sup> Results of dose-dependent photolysis experiments conducted at 206 nm are in good agreement with those performed at 254 nm. Ion counts of products assigned to  $m/z = 30, 31, 44, 45, 46, 57, 58, 59, 89, 117,$  and 118 decreases, while those of species at  $m/z = 97, 101, 119, 128, 130, 146,$  and 191 increase at low dose ( $0.9 \pm 0.1$  eV molecule<sup>-1</sup>).

**3.3. Proposed Decomposition Mechanisms.** Here we propose the underlying photodecomposition pathways of RDX involved in the formation of the aforementioned products by comparing our experimental findings (Figures 9 and 10) with previous electronic structure calculations as discussed below. The RDX molecules are electronically excited when exposed to UV light. Gas phase calculations suggest that excited molecules may relax from higher electronic states ( $S_1, S_2$ ) nonadiabatically through a series of conical intersections to the ground state of RDX–nitrite ( $S_0$  RDX-ONO), via nitro–nitrite isomer-

ization and eventually dissociate from the  $S_0$  RDX-ONO state via O–NO bond cleavage.<sup>7,46</sup>

The process of nitro–nitrite isomerization through conical intersections is barrierless and hence highly favorable. Excited molecules could also relax through nonradiative transition from the higher electronic states ( $S_1, S_2$ ) to higher vibrational levels of its ground state ( $S_0$  RDX-NO<sub>2</sub>) and finally dissociate from its  $S_0$  RDX-NO<sub>2</sub> state following three primary reaction channels: (i) N–NO<sub>2</sub> bond fission, (ii) HONO elimination, and (iii) C–N bond cleavage. The calculated energy barriers for the N–NO<sub>2</sub> fission (163 kJ mol<sup>-1</sup>) and HONO elimination (164 kJ mol<sup>-1</sup>) are lower than that for C–N bond rupture, and hence the former two channels are more favorable at the ground state.<sup>35</sup> On the basis of these mechanisms, we have proposed probable reaction channels in parts a and b of Figures 11 that could occur after electronic excitation of RDX. In Figure 11a, we depict reactions channels that could initiate due to N–NO<sub>2</sub> fission, C–N bond rupture, and HONO-elimination at the ground state of RDX; these reactions have been previously proposed through theoretical calculations<sup>35–37,41,42</sup> and certainly rationalize the products observed in our experiments.

**3.3.1. N–NO<sub>2</sub> Fission Channel.** The first NO<sub>2</sub> bond fission of RDX (1) leads to a cyclic aminyl radical, 2a ( $C_3H_6N_5O_4$ ; 176 amu) and nitrogen dioxide, 3 (NO<sub>2</sub>; 46 amu); this requires an energy of 163 kJ mol<sup>-1</sup>.<sup>35</sup> The later (NO<sub>2</sub>) can decompose to nitrogen monoxide, 4 (NO; 30 amu), via N–O bond cleavage. Radical 2a ( $C_3H_6N_5O_4$ ; 176 amu) can undergo a second N–NO<sub>2</sub> bond fission followed by 1,2-hydrogen shift to yield a mononitro product, 5b ( $C_3H_6N_4O_2$ ; 130 amu) after crossing an energy barrier of 187.4 kJ mol<sup>-1</sup>; this pathway was predicted computationally by Goddard and co-workers.<sup>35</sup> Alternatively, intermediate 5a can also accept two hydrogen atoms to form a cyclic mononitro product, 6 ( $C_3H_8N_4O_2$ ; 132 amu). This mononitro moiety (6) may encounter N–NO<sub>2</sub> fission followed by hydrogen addition leading to 1,3,5-triazinane, 8 ( $C_3H_9N_3$ ; 87). Products corresponding to the molecular masses of 130 ( $C_3H_6N_4O_2$ ), 87 ( $C_3H_9N_3$ ), and 46 (NO<sub>2</sub>) amu were observed in our experiments, signifying a high probability of N–NO<sub>2</sub> fission(s) of RDX. It is intriguing to note that species holding  $m/z = 130$  and 87 were not observed in the mass spectrum when exposed to 254 nm light at the lowest dose ( $0.10 \pm 0.02$  eV molecule<sup>-1</sup>; Figure 9). On the contrary these species ( $m/z = 130$  and 87) were detected upon photolysis at 206 nm light at the lowest dose ( $0.20 \pm 0.02$  eV molecule<sup>-1</sup>, Figure 10). This finding may indicate that pathways leading to products holding masses 130 and 87 amu, i.e., N–NO<sub>2</sub> fission of radical 2a followed by a 1,2-hydrogen shift or hydrogen addition, are (preferentially) formed at higher photon energy.

**3.3.2. C–N Bond Rupture Channel.** The cyclic aminyl radical, 2a ( $C_3H_6N_5O_4$ ; 176 amu), could undergo a C–N bond rupture to form an acyclic intermediate, 2b ( $C_3H_6N_5O_4$ ; 176 amu), via a barrier of 110 kJ mol<sup>-1</sup>.<sup>35,37</sup> This radical (2b) may encounter a second C–N bond cleavage which has an energy barrier of 103 kJ mol<sup>-1</sup>, to yield a mononitro N-centered radical, 9 ( $C_2H_4N_3O_2$ ; 102 amu), and methylene nitramine, 10 (CH<sub>2</sub>NNO<sub>2</sub>; 74 amu). Chakraborty et al. predicted this reaction sequence via *ab initio* calculations.<sup>35</sup> Radical 9 can eliminate a hydrogen atom to generate a mononitro product, 11 ( $C_2H_3N_3O_2$ ; 101 amu). Radical intermediate 9 ( $C_2H_4N_3O_2$ ) could undergo cyclization followed by elimination of N<sub>2</sub>O to generate an oxygen-

centered radical, **13** ( $C_2H_4NO^\bullet$ ); this pathway was predicted by Thynell and co-workers through quantum chemical calculations.<sup>67</sup> This radical, **13**, may accept a hydrogen atom leading to a product having mass 59 amu ( $C_2H_5NO$ ; **14a**), which is observed in the experiment.

Intermediate **2b** may further undergo a hydrogen-shift to form yet another acyclic carbon-centered radical, **2c** ( $C_3H_6N_5O_4^\bullet$ ); this process requires an energy of 36 kJ mol<sup>-1</sup>. Radical intermediate **2c** dissociates to yet another carbon-centered radical, **15** ( $C_2H_5N_4O_4^\bullet$ ; 149 amu), and a hydrogen cyanide molecule (HCN) after crossing a barrier of 68 kJ mol<sup>-1</sup>; this pathway was proposed by Chakraborty et al. and Schweigert through ab initio calculation.<sup>35</sup> This radical ( $C_2H_5N_4O_4^\bullet$ ; **15**) may eliminate a NO<sub>2</sub> molecule via N–NO<sub>2</sub> fission to yield a stable intermediate, **16** ( $C_2H_5N_3O_2$ ; 103 amu),<sup>37</sup> which can accept two hydrogen atoms to form the product **17** ( $C_2H_7N_3O_2$ ; 105 amu). The latter (**17**) could experience yet another C–N bond cleavage leading to methylamine, **18** ( $CH_3NH_2$ ; 31 amu) and methylene nitramine, **10** ( $CH_2NNO_2$ ; 74 amu). Intermediate **16** could also dissociate to N-centered radical, **19** ( $C_2H_5N^\bullet$ ) via N–NO<sub>2</sub> fission; this radical could undergo C–N scission to form methylenimine ( $CH_3N$ ; **20**).<sup>37</sup> Addition of two hydrogen atoms to methylenimine could lead to its hydrogenated counterpart methylamine ( $CH_3NH_2$ ; **18**), which has been observed in the experiment. Radical **19** could also accept a hydrogen radical to form the product, **21a** ( $C_2H_6N_2$ ), holding mass 58 amu. The resulting methylene nitramine ( $CH_2NNO_2$ ; **10**) molecules may dissociate to dinitrogen monoxide, **22** ( $N_2O$ ; 44 amu), and formaldehyde, **23** ( $H_2CO$ ; 30 amu). The N<sub>2</sub>O molecule may react with the  $CH_2N^\bullet$  radical to produce diazomethane ( $CH_2NN$ ). This reaction pathway was predicted by Goddard and co-workers based on theoretical calculations.<sup>41</sup> Furthermore, the diazomethane ( $CH_2NN$ ) molecules could undergo a hydrogen addition reaction to generate methane diazene ( $CH_3NNH$ ). H<sub>2</sub>CO (formaldehyde) either dissociates to CO (carbon monoxide; **26**; 28 amu) and hydrogen and/or it reacts with another formaldehyde molecule to form ketene, **27** ( $H_2CCO$ ; 42 amu), and water ( $H_2O$ ; 18 amu). The later pathway, i.e., formation of ketene was predicted computationally and verified experimentally in our previous study.<sup>44</sup> The detection of products holding masses of 105, 101, 74, 58, 59, 42, and 31 amu in our experiment (Figure 9) further validates the likelihood of the C–N bond rupture channel in the UV decomposition of RDX. The existence of these masses also reveals evidence of reactive radical intermediates such as  $C_2H_4N_3O_2^\bullet$  (**9**),  $C_2H_4NO^\bullet$  (**13**),  $C_2H_5N_4O_4^\bullet$  (**15**), and  $C_2H_5N^\bullet$  (**19**), which have been predicted only through ab initio calculations.<sup>35,37,67</sup> Interestingly, ion signals at  $m/z = 105$  and 58 are not observed as the result of RDX photolysis at 206 nm; signals at  $m/z = 105$  and 58 are rather distinct when exposed to 254 nm light even at the low dose (Figure 9). This finding implies that the underlying reaction mechanism yielding products corresponding to masses 105 and 58 amu is open at lower photon energy. On the other hand, reaction channel leading to a product of mass 59 amu appears to be more favorable at higher photon energy, since the signal at  $m/z = 59$  is distinct when RDX is exposed to 206 nm light even at a low dose, while this signal is absent in a similar experiment (low dose) conducted at 254 nm.

**3.3.3. HONO Elimination Channel.** Molecular elimination of nitrous acid (HONO) could also initiate RDX decomposition. The first molecular HONO elimination results in the

formation of a dinitro intermediate, **28** ( $C_3H_5N_5O_4$ ; 175 amu), which can subsequently undergo a second HONO elimination to generate a cyclic mononitro product, **29** ( $C_3H_4N_4O_2$ ; 128 amu). This product (**29**) may encounter yet a third HONO elimination yielding 1,3,5-triazine, **30** ( $C_3H_3N_3$ ; 81 amu). Gas phase calculations performed by Goddard and co-workers identified the HONO elimination pathway to be energetically most favorable for the formation of triazine ( $C_3H_3N_3$ ; 81 amu).<sup>35</sup> Our observation of species holding masses at 128 and 81 amu are indicative of the HONO elimination channel occurring during the UV photolysis of RDX. It is intriguing to recall that the ion signal at  $m/z = 81$  is not observed in the ReTOF-MS data after photodecomposition at 206 nm. However, the signal at  $m/z = 81$  is observed when irradiated at 254 nm even in the low dose experiment. This observation proposes that HONO elimination from product **29** ( $C_3H_4N_4O_2$ ; 128 amu) leading to 1,3,5-triazine (81 amu) is preferable at lower photon energy. At higher photon energy (206 nm), a mononitro product holding mass 128 amu ( $C_3H_4N_4O_2$ ) may follow the HONO elimination pathway instead of the HONO elimination channel and generate oxy-sym-triazine, **31** ( $C_3H_3N_3O$ ; 97 amu).

**3.3.4. Bimolecular Reaction with Nitrogen Monoxide (NO).** Once the concentration of nitrogen monoxide (NO) molecules increases, NO may react with residual (unreacted) RDX molecules to produce a mononitroso analogue of RDX, **32**, i.e., 1-nitroso-3,5-hexahydro-*s*-triazine (ONDNTA;  $C_3H_6N_6O_5$ ). Such reactions have been proposed previously in the condensed phase.<sup>8,67</sup> ONDNTA may decompose via HONO elimination followed by C–N bond rupture to yield a mononitroso product *N*-methylene nitrousamide, **21b** ( $CH_2N_2O$ ; 58 amu), and a mononitro product, **11** ( $C_2H_3N_3O_2$ ; 101 amu). This pathway has been computationally explored by Thynell and co-workers.<sup>67</sup> ONDNTA could also lead to mononitroso intermediates such as  $C_2H_2N_4O$  (98 amu); this has been previously discussed in ref 15.

**3.3.5. Nitro–Nitrite Isomerization Channel.** After electronic excitation, the excited RDX molecules may reach the ground state of RDX–nitrite ( $S_0$  RDX–ONO) from the excited electronic states ( $S_1/S_2$ ) via conical intersections. The barrierless nature of this nonadiabatic pathway makes it highly favorable. It is important to mention that nitro–nitrite isomerization from the ground state of RDX ( $S_0$  RDX–NO<sub>2</sub>) is unfavorable due to a very high energy barrier (386 kJ mol<sup>-1</sup>).<sup>7</sup> Once the excited RDX molecule relaxes to the ground state of RDX–nitrite ( $S_0$  RDX–ONO), it could dissociate via multiple fragmentation channels<sup>7</sup> for example, NO elimination, N–NO<sub>2</sub> fission, HONO elimination, and C–N bond rupture (see Figure 11b). Excited state potential energy surfaces (PES) explored computationally by Bernstein and co-workers revealed that elimination of nitrogen monoxide (NO) from the ground state of RDX–nitrite via O–NO bond fission requires an energy of 29 kJ mol<sup>-1</sup>.<sup>7,46</sup> On the other hand, dissociation of RDX to nitrogen dioxide (NO<sub>2</sub>) from its ground state ( $S_0$  RDX–NO<sub>2</sub>) via N–NO<sub>2</sub> fission requires an energy of at least 163 kJ mol<sup>-1</sup>.<sup>35</sup> Thus, elimination of NO is more facile after the RDX molecule has isomerized to its nitrite form following electronic excitation. This theory supports our experimental observation of higher concentration of NO relative to NO<sub>2</sub> in the IR (Figures 1 and 2) and mass spectra, even at the low dose experiments (Figures 9 and 10) suggesting that the nitro–nitrite isomerization occurred at the initial stage of decomposition.

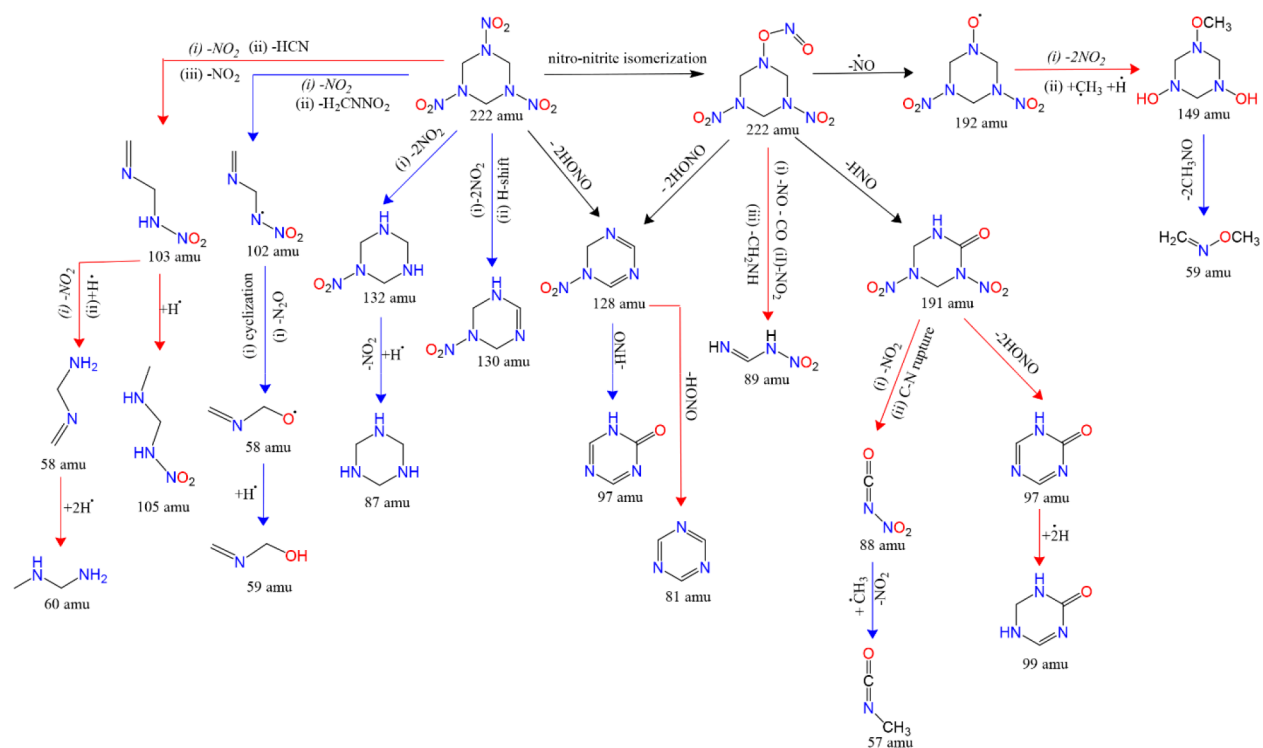


**Figure 12.** Wavelength-selective decomposition pathways of RDX. Channels leading to products at 130, 87, 59, and 57 amu are preferable at a higher photon energy (denoted through blue color arrows). Pathways leading to products at 149, 105, 99, 89, 88, 81, 60, and 58 amu are more favorable at a lower photon energy (represented through red color arrows).

Following nitro–nitrite isomerization, RDX could also undergo HONO elimination. The first HONO elimination would result in formation of a dinitro intermediate, **28** ( $C_3H_5N_5O_4$ ; 175 amu). Subsequent elimination of second and third HONO molecules would generate a mononitro product, **29** ( $C_3H_4N_4O_2$ ; 128 amu), and 1,3,5-triazine, **30** ( $C_3H_3N_3$ ; 81 amu), respectively. Intermediate **1a** can also decompose through a concerted elimination of HNO, yielding a dinitro product, **34** ( $C_3H_5N_5O_5$ ; 191 amu). This product undergoes N–NO<sub>2</sub> fission to form an N-centered radical, **35a** ( $C_3H_5N_4O_3^{\bullet}$ ; 145 amu), which can readily accept a hydrogen atom to produce a mononitro product, **36** ( $C_3H_6N_4O_3$ ; 146 amu). The cyclic intermediate **35a** ( $C_3H_5N_4O_3^{\bullet}$ ; 145 amu) could engage in ring opening reaction via C–N bond rupture to form an acyclic N-centered radical, **35b** ( $C_3H_5N_4O_3^{\bullet}$ ; 145 amu). A radical intermediate, **35b**, may undergo yet another C–N bond breakage, which results in elimination of methylene nitramine ( $CH_2NNO_2$ ; 74 amu) and formation of a nitrogen-centered radical, **37** ( $C_2H_3N_2O^{\bullet}$ ; 71). Radical **37** subsequently could accept a hydrogen atom to lead to a product *N*-methylene acetamide, **38** ( $C_2H_4N_2O$ ; 72 amu). Products holding masses 72 and 146 are observed in the mass spectrum. It is important to note here that elimination of HONO and HNO is highly likely since the oxygen atom of the nitrite group (–ONO) could easily interact with the neighboring hydrogen atom of the RDX ring. Electronic structure calculations also suggest that, during the nitro–nitrite isomerization, the NO<sub>2</sub> group at the active site interacts with the remainder of the molecule from a distance of 2.9 Å.<sup>7</sup>

The oxy-*sym*-triazine (OST) molecule, **31** ( $C_3H_3N_3O$ ; 97 amu), can emerge from the dinitro product, **34** ( $C_3H_5N_5O_5$ ; 191 amu), via two successive HONO eliminations. The former product (OST;  $C_3H_3N_3O$ ) can further accept two hydrogen

atoms to form **39** ( $C_3H_5N_3O$ ; 99 amu). Although product holding mass 97 amu ( $C_3H_3N_3O$ ; **31**) is observed during photolysis at 206 nm, the signature of its hydrogenated counterpart; i.e., a product corresponding to mass 99 amu ( $C_3H_5N_3O$ ; **39**) is not observed at 206 nm photolysis. Interestingly, ion signals corresponding to both the masses ( $m/z = 97$  and  $99$ ) are observed at 254 nm implying that formation of product **39** ( $C_3H_5N_3O$ ; 99 amu) from **34** ( $C_3H_5N_5O_5$ ; 191 amu) through consecutive HONO elimination and hydrogen addition is preferred at lower photon energy. At higher photon energy, oxy-*sym*-triazine (97 amu) may originate via HNO elimination from product **29** ( $C_3H_4N_4O_2$ ; 128 amu) as discussed above. **34** may dissociate to product *N*-nitro isocyanate, **40** ( $CN_2O_3$ ; 88 amu), via intermediates, **35c** ( $c-C_3H_5N_4O_3^{\bullet}$ ; 145 amu) and **35d** ( $C_3H_5N_4O_3^{\bullet}$ ; 145 amu), after consecutive N–NO<sub>2</sub> and C–N bond rupture. The *N*-nitro isocyanate **40** ( $CN_2O_3$ ; 88 amu) may undergo N–NO<sub>2</sub> fission followed by addition of a methyl radical ( $\bullet CH_3$ ) to produce *N*-methyl isocyanate product, **41** ( $C_2H_3NO$ ; 57 amu). It is worth to recall that product at  $m/z = 57$  is not observed during photolysis of RDX at 254 nm; on the other hand, this product is detected when RDX is exposed to 206 nm light even at the lowest dose ( $0.20 \pm 0.02$  eV molecule<sup>-1</sup>; Figure 10). On the basis of this observation, we may propose that the aforementioned pathway leading to a product holding a molecular mass of 57 amu ( $C_2H_3NO$ ) is more favorable at a higher photon energy. Product **40** ( $CN_2O_3$ ; 88 amu) could decompose rapidly to **41** ( $C_2H_3NO$ ; 57 amu) at higher photon energy, therefore, the ion signal corresponding to  $m/z = 88$  is not observed at 206 nm irradiation. Two consecutive C–N bond ruptures of dinitro moiety **34** ( $C_3H_5N_5O_5$ ; 191 amu) may generate a C, N-centered biradical, **42** ( $C_2H_4N_4O_4^{\bullet\bullet}$ ; 148 amu), which

dissociates to two molecules of methylene nitramine, ( $\text{CH}_2\text{NNO}_2$ , 74 amu) following another C–N bond cleavage. Alternatively, biradical **42** ( $\text{C}_2\text{H}_4\text{N}_4\text{O}_4^{\bullet\bullet}$ ; 148 amu) may encounter a 1,2-hydrogen shift to form a dinitro intermediate, **44** ( $\text{C}_2\text{H}_4\text{N}_4\text{O}_4$ ; 148 amu). This intermediate (**44**) reacts to develop a mononitro product, **45** ( $\text{C}_3\text{H}_7\text{N}_3\text{O}_2$ ; 117 amu), via N–NO<sub>2</sub> fission and addition of a methyl radical ( $\bullet\text{CH}_3$ ).

The nitro–nitrite isomerization process could be followed by a concerted elimination of NO (nitrogen monoxide) and CO (carbon monoxide) yielding a nitrogen-centered radical, **46** ( $\text{C}_2\text{H}_6\text{N}_5\text{O}_2^{\bullet}$ ; 164 amu), which may experience a N–NO<sub>2</sub> fission generating yet another biradical, **47a** ( $\text{C}_2\text{H}_6\text{N}_4\text{O}_2^{\bullet\bullet}$ ; 118 amu). Biradical **47a** undergoes a 1,2-hydrogen shift to form an acyclic mononitro product, **41b** ( $\text{C}_2\text{H}_6\text{N}_4\text{O}_2$ ), corresponding to mass 118 amu, which has been observed in the experiment. Biradical **47a** may dissociate into a mononitro product, **48** ( $\text{CH}_3\text{N}_3\text{O}_2$ ; 89 amu), and methanimine ( $\text{CH}_2\text{NH}$ ) via C–N bond cleavage. Interestingly, the signal at  $m/z = 89$  disappears during the photolysis with 206 nm photons (Figure 10). However, this product is observed during photodissociation at 254 nm even at the lowest dose of  $0.10 \pm 0.02$  eV molecule<sup>-1</sup> (Figure 9). This suggests that the reaction pathway leading to product **48** ( $\text{CH}_3\text{N}_3\text{O}_2$ ; 89 amu) could be feasible only at a lower photon energy. The HONO elimination from mononitro product **47b** would yield a diamine product, **49** ( $\text{C}_2\text{H}_5\text{N}_3$ ; 71 amu). Addition of two hydrogen atoms to a diamine moiety (**49**) could generate its hydrogenated counterpart, **50** ( $\text{C}_2\text{H}_7\text{N}_3$ ; 73 amu). Alternatively, product **42** may accept four hydrogen atoms to form an amine moiety, **51** ( $\text{C}_2\text{H}_9\text{N}_3$ ; 75 amu).

After the nitro–nitrite isomerization, **1a** may eliminate NO (nitrogen monoxide) to form an oxygen-centered (aminoxyl) radical **52** ( $\text{C}_3\text{H}_6\text{N}_5\text{O}_5^{\bullet}$ ; 192 amu). The aminoxyl radical ( $\text{C}_3\text{H}_6\text{N}_5\text{O}_5^{\bullet}$ ) has been detected via electron spin resonance (ESR) technique by Darnez et al. during photolysis of RDX at 254 nm.<sup>82,83</sup> Calculations reveal that this reaction has an energy barrier of close to 29 kJ mol<sup>-1</sup>.<sup>7</sup> Radical intermediate **52** could further dissociate to methylene nitramine ( $\text{CH}_2\text{NNO}_2$ ) and a carbon-centered radical, **47c** ( $\text{C}_2\text{H}_4\text{N}_3\text{O}_3^{\bullet}$ ; 118 amu), via C–N bond cleavage. Radical **47c** could decompose to methylene nitramine and a mononitroso radical, **53** ( $\text{CH}_2\text{NO}^{\bullet}$ ; 44 amu), following another C–N bond rupture. The latter (mononitroso radical; **53**) can rapidly accept a hydrogen atom to form product **54** ( $\text{CH}_3\text{NO}$ ; 45 amu) which is observed in the experiment. Radical **47c** could also accept a hydrogen atom to yield a nitro–nitroso product, **55** ( $\text{C}_2\text{H}_5\text{N}_3\text{O}_3$ ; 119 amu), which is detected in our mass spectrum. A product holding mass 149 amu ( $\text{C}_4\text{H}_{11}\text{N}_3\text{O}_3$ ; **58**) may originate from an aminoxyl radical via intermediate **56** followed by bimolecular addition reaction with methyl ( $\bullet\text{CH}_3$ ) and hydrogen radicals. This product (**58**) could further dissociate to species **54** ( $\text{CH}_3\text{NO}$ ; 45 amu) and **14b** ( $\text{C}_2\text{H}_5\text{NO}$ ; 59 amu) via triple C–N bond cleavage. Products corresponding to these three masses, 149, 45, and 59 amu, are observed in the mass spectrum.

The wavelength-selective decomposition pathways of RDX are summarized in Figure 12. Channels leading to products corresponding to masses 130, 87, 59, and 57 amu are preferable at a higher photon energy (206 nm, 6.02 eV), while pathways leading to species at 149, 105, 99, 88, 89, 81, 60, and 58 amu are favorable at a lower photon energy (254 nm, 4.88 eV). These products might be considered as tracers of a wavelength-dependent photolysis of RDX. Overall, RDX

could dissociate via N–NO<sub>2</sub> fission, HONO elimination, nitro–nitrite isomerization, and C–N bond rupture channels when exposed to UV light. The N–NO<sub>2</sub> fission and nitro–nitrite isomerization channels appear to be more dominant at the early stage of decomposition. The N–NO<sub>2</sub> fission channel yields products at 130, 87, 46, and 30 amu, whereas the HONO elimination channel generates products at 128, 97, and 81 amu, while the C–N rupture pathway following N–NO<sub>2</sub> fission leads to species holding masses 105, 101, 59, 58, 74, 44, 42, and 31. Nitro–nitrite isomerization in conjunction with successive reaction pathways is proposed to generate a variety of products including at 191, 146, 149, 117, 118, 119, 88, 71, 72, 73, 74, 75, 60, 59, 45, and 30 amu as discussed above. Our experimental observations suggest that besides the N–NO<sub>2</sub> fission, the nitro–nitrite isomerization could also play a major role to trigger the decomposition of RDX after electronic excitation. Most of the previously reported computational analyses address the thermal decomposition of RDX from its electronic ground state via N–NO<sub>2</sub>, HONO elimination, C–N bond rupture or bimolecular reactions.<sup>35,37,41,42,67</sup> UV-photolysis of RDX is more complex as it involves excited state dynamics and ground states along with conical intersections. To the best of our knowledge, as of now, there has been no reported computational study that explores the excited-state potential energy surfaces of condensed-phase RDX.

#### 4. CONCLUSIONS

In summary, the UV photodissociation of solid-phase RDX performed at 5 K exploiting different wavelengths (254 (4.88 eV), 236 (5.25 eV), 222 (5.58 eV), and 206 (6.02 eV) nm) and doses revealed a wide spectrum of photoproducts. Evidence of simple decomposition products such as CO<sub>2</sub>, N<sub>2</sub>O, CO, HCO, H<sub>2</sub>O, NO, (NO)<sub>2</sub>, N<sub>2</sub>O<sub>3</sub>, and the nitrite group (–ONO) were captured by FTIR spectroscopy in the condensed-phase during the photolysis. PI-ReTOF-MS collected during the warmup-phase identified 32 cyclic and acyclic products at  $m/z$  values ranging from 30 to 191. Low dose experiments suggest that NO and N<sub>2</sub>O<sub>3</sub> products rapidly develop during the initial stage of the decomposition relative to CO<sub>2</sub>, N<sub>2</sub>O, CO, and H<sub>2</sub>O implying that N–NO<sub>2</sub> and nitro–nitrite isomerization could be the initial steps in the decomposition of RDX molecules following electronic excitation. Products observed at  $m/z$  values of 59, 72, 73, 88, 99, 117, 118, 119, 146, 149, and 191 were detected for the first time in photolysis experiments. Among those, products at  $m/z = 191$ , 149, 146, 119, and 72 are primary products which likely originate via nitro–nitrite isomerization. Wavelength-dependent studies revealed that pathways leading to products holding masses 130, 87, 59, and 57 amu are more prominent at a higher photon energy while reaction mechanisms yielding products of masses 149, 105, 99, 81, 89, 58, and 60 amu are favorable at a lower photon energy (Figure 12). Finally, the decomposition mechanisms reported through gas-phase and condensed-phase calculations<sup>7,34,35,37,41</sup> were exploited to rationalize the formation of the observed species. Further experiments are planned, exploiting isomer-selective photoionization<sup>44,84,85</sup> to explicitly verify the structures of the decomposition products and hence the nature of the isomer(s) formed. Experimental results will be combined with theoretical simulations to unravel the complex decomposition pathways of RDX.

## ■ ASSOCIATED CONTENT

## SI Supporting Information

The Supporting Information is available free of charge at <https://pubs.acs.org/doi/10.1021/acs.jpca.0c05726>.

Experimental setup scheme, UV–vis spectrum, NMR spectra, IR spectra, mass spectrum, and column densities (PDF)

## ■ AUTHOR INFORMATION

## Corresponding Author

Ralf I. Kaiser – Department of Chemistry and W. M. Keck Research Laboratory in Astrochemistry, University of Hawaii, Honolulu, Hawaii 96822, United States; [orcid.org/0000-0002-7233-7206](https://orcid.org/0000-0002-7233-7206); Email: [ralfk@hawaii.edu](mailto:ralfk@hawaii.edu)

## Authors

Santosh K. Singh – Department of Chemistry and W. M. Keck Research Laboratory in Astrochemistry, University of Hawaii, Honolulu, Hawaii 96822, United States

Vasant Vuppuluri – Mechanical Engineering, Purdue Energetics Research Center, Purdue University, West Lafayette, Indiana 47907, United States

Steven F. Son – Mechanical Engineering, Purdue Energetics Research Center, Purdue University, West Lafayette, Indiana 47907, United States

Complete contact information is available at: <https://pubs.acs.org/doi/10.1021/acs.jpca.0c05726>

## Notes

The authors declare no competing financial interest.

## ■ ACKNOWLEDGMENTS

This project was supported by the U.S. Army Research Office (ARO) (W911NF1810438).

## ■ REFERENCES

- (1) Adams, G. F.; Shaw, R. W. Chemical reactions in energetic materials. *Annu. Rev. Phys. Chem.* **1992**, *43*, 311–340.
- (2) *Chemistry of Energetic Materials*; Olah, G.; Squire, D. R., Eds.; Academic Press: San Diego, CA, 1991.
- (3) Bulusu, S. N. *Chemistry and Physics of Energetic Materials* **1990**, DOI: 10.1007/978-94-009-2035-4.
- (4) Greenfield, M.; Guo, Y. Q.; Bernstein, E. R. Ultrafast photodissociation dynamics of HMX and RDX from their excited electronic states via femtosecond laser pump–probe techniques. *Chem. Phys. Lett.* **2006**, *430*, 277–281.
- (5) Guo, Y. Q.; Greenfield, M.; Bhattacharya, A.; Bernstein, E. R. On the excited electronic state dissociation of nitramine energetic materials and model systems. *J. Chem. Phys.* **2007**, *127*, 154301.
- (6) Im, H.-S.; Bernstein, E. R. On the initial steps in the decomposition of energetic materials from excited electronic states. *J. Chem. Phys.* **2000**, *113*, 7911–7918.
- (7) Bhattacharya, A.; Bernstein, E. R. Nonadiabatic decomposition of gas-phase RDX through conical intersections: An ONIOM-CASSCF study. *J. Phys. Chem. A* **2011**, *115*, 4135–4147.
- (8) Behrens, R.; Bulusu, S. Thermal decomposition of energetic materials. 3. Temporal behaviors of the rates of formation of the gaseous pyrolysis products from condensed-phase decomposition of 1,3,5-trinitrohexahydro-s-triazine (RDX). *J. Phys. Chem.* **1992**, *96*, 8877–8891.
- (9) Behrens, R.; Bulusu, S. Thermal decomposition of energetic materials. 4. Deuterium isotope effects and isotopic scrambling (H/D, <sup>13</sup>C/<sup>18</sup>O, <sup>14</sup>N/<sup>15</sup>N) in condensed-phase decomposition of 1,3,5-trinitrohexahydro-s-triazine (RDX). *J. Phys. Chem.* **1992**, *96*, 8891–8897.
- (10) Zhao, X.; Hints, E. J.; Lee, Y. T. Infrared multiphoton dissociation of RDX in a molecular beam. *J. Chem. Phys.* **1988**, *88*, 801–810.
- (11) Zuckermann, H.; Greenblatt, G. D.; Haas, Y. Hydroxyl radical formation in the infrared multiphoton decomposition of jet-cooled cyclic nitroamines. *J. Phys. Chem.* **1987**, *91*, 5159–5161.
- (12) Maharrey, S.; Behrens, R. Thermal decomposition of energetic materials. 5. Reaction processes of 1,3,5-trinitrohexahydro-s-triazine below its melting point. *J. Phys. Chem. A* **2005**, *109*, 11236–11249.
- (13) Miao, M.; Dreger, Z. A.; Patterson, J. E.; Gupta, Y. M. Shock wave induced decomposition of RDX: Quantum chemistry calculations. *J. Phys. Chem. A* **2008**, *112*, 7383–7390.
- (14) Botcher, T. R.; Wight, C. A. Transient thin film laser pyrolysis of RDX. *J. Phys. Chem.* **1993**, *97*, 9149–9153.
- (15) Singh, S. K.; Zhu, C.; Vuppuluri, V.; Son, S. F.; Kaiser, R. I. Probing the reaction mechanisms involved in the decomposition of solid 1,3,5-trinitro-1,3,5-triazinane by energetic electrons. *J. Phys. Chem. A* **2019**, *123*, 9479–9497.
- (16) Alix, J.; Collins, S. The photochemistry of RDX in solid argon at 10 K. *Can. J. Chem.* **1991**, *69*, 1535–1538.
- (17) Östmark, H.; Bergman, H.; Ekvall, K. Laser pyrolysis of explosives combined with mass spectral studies of the ignition zone. *J. Anal. Appl. Pyrolysis* **1992**, *24*, 163–178.
- (18) Makarov, I. E.; Zhestkova, T. P.; Zhukova, T. N. Radiation-induced decomposition of cyclotrimethylenetrinitramine in aqueous solutions. *High Energy Chem.* **2011**, *45*, 89–92.
- (19) Zhang, W.; Shen, R.; Ye, Y.; Wu, L.; Hu, Y.; Zhu, P. Dissociation of cyclotrimethylenetrinitramine under 1064-nm laser irradiation investigated by time-of-flight mass spectrometer. *Spectrosc. Lett.* **2014**, *47*, 611–615.
- (20) Lee, Y.; Tang, C.-J.; Litzinger, T. A. A study of the chemical and physical processes governing CO<sub>2</sub> laser-induced pyrolysis and combustion of RDX. *Combust. Flame* **1999**, *117*, 600–628.
- (21) Gongwer, P. E.; Brill, T. B. Thermal decomposition of energetic materials 73: the identity and temperature dependence of “minor” products from flash-heated RDX. *Combust. Flame* **1998**, *115*, 417–423.
- (22) Capellos, C.; Papagiannakopoulos, P.; Liang, Y.-L. The 248 nm photodecomposition of hexahydro-1,3,5-trinitro-1,3,5-triazine. *Chem. Phys. Lett.* **1989**, *164*, 533–538.
- (23) Tang, T. B.; Chaudhri, M. M.; Rees, C. S.; Mullock, S. J. Decomposition of solid explosives by laser irradiation: A mass spectrometric study. *J. Mater. Sci.* **1987**, *22*, 1037–1044.
- (24) Dang, N. C.; Gottfried, J. L.; De Lucia, F. C. Energetic material response to ultrafast indirect laser heating. *Appl. Opt.* **2017**, *56*, B85–B91.
- (25) Gares, K. L.; Bykov, S. V.; Brinzer, T.; Asher, S. A. Solution and solid hexahydro-1,3,5-trinitro-1,3,5-triazine (RDX) ultraviolet (UV) 229 nm photochemistry. *Appl. Spectrosc.* **2015**, *69*, 545–554.
- (26) Dickinson, J. T.; Jensen, L. C.; Doering, D. L.; Yee, R. Mass spectroscopy study of products from exposure of cyclotrimethylene-trinitramine single crystals to KrF excimer laser radiation. *J. Appl. Phys.* **1990**, *67*, 3641–3651.
- (27) Lemire, G. W.; Simeonsson, J. B.; Sausa, R. C. Monitoring of vapor-phase nitro compounds using 226-nm radiation: fragmentation with subsequent NO resonance-enhanced multiphoton ionization detection. *Anal. Chem.* **1993**, *65*, 529–533.
- (28) Wynn, C. M.; Palmacci, S.; Kunz, R. R.; Clow, K.; Rothschild, M. Detection of condensed-phase explosives via laser-induced vaporization, photodissociation, and resonant excitation. *Appl. Opt.* **2008**, *47*, 5767–5776.
- (29) Brill, T. B.; Beckstead, M. C.; Flanagan, J. E.; Lin, M. C.; Litzinger, T. A.; Waesche, R. H. W.; Wight, C. A. Chemical speciation and dynamics in the surface combustion zone of energetic materials. *J. Propul. Power* **2002**, *18*, 824–834.

- (30) Cosgrove, J. D.; Owen, A. J. The thermal decomposition of 1,3,5-trinitrohexahydro-1,3,5-triazine (RDX). *Chem. Commun. (London)* **1968**, 286–286.
- (31) Cosgrove, J. D.; Owen, A. J. The thermal decomposition of 1,3,5 trinitro hexahydro 1,3,5 triazine (RDX)—part I: The products and physical parameters. *Combust. Flame* **1974**, *22*, 13–18.
- (32) Batten, J. The thermal decomposition of RDX at temperatures below the melting point. III. Towards the elucidation of the mechanism. *Aust. J. Chem.* **1971**, *24*, 945–954.
- (33) Wu, C. J.; Fried, L. E. Ab initio study of RDX decomposition mechanisms. *J. Phys. Chem. A* **1997**, *101*, 8675–8679.
- (34) Molt, R. W.; Watson, T.; Bazanté, A. P.; Bartlett, R. J.; Richards, N. G. J. Gas phase RDX decomposition pathways using coupled cluster theory. *Phys. Chem. Chem. Phys.* **2016**, *18*, 26069–26077.
- (35) Chakraborty, D.; Muller, R. P.; Dasgupta, S.; Goddard, W. A. The mechanism for unimolecular decomposition of RDX (1,3,5-Trinitro-1,3,5-triazine), an ab initio study. *J. Phys. Chem. A* **2000**, *104*, 2261–2272.
- (36) Swadley, M. J.; Li, T. Reaction mechanism of 1,3,5-trinitro-s-triazine (RDX) deciphered by density functional theory. *J. Chem. Theory Comput.* **2007**, *3*, 505–513.
- (37) Schweigert, I. V. Ab initio molecular dynamics of high-temperature unimolecular dissociation of gas-phase RDX and its dissociation products. *J. Phys. Chem. A* **2015**, *119*, 2747–2759.
- (38) Sharia, O.; Kuklja, M. M. Ab initio kinetics of gas phase decomposition reactions. *J. Phys. Chem. A* **2010**, *114*, 12656–12661.
- (39) Harris, N. J.; Lammertsma, K. Ab initio density functional computations of conformations and bond dissociation energies for hexahydro-1,3,5-trinitro-1,3,5-triazine. *J. Am. Chem. Soc.* **1997**, *119*, 6583–6589.
- (40) Shalashilin, D. V.; Thompson, D. L. Monte carlo variational transition-state theory study of the unimolecular dissociation of RDX. *J. Phys. Chem. A* **1997**, *101*, 961–966.
- (41) Strachan, A.; Kober, E. M.; van Duin, A. C. T.; Oxgaard, J.; Goddard, W. A., III Thermal decomposition of RDX from reactive molecular dynamics. *J. Chem. Phys.* **2005**, *122*, 054502.
- (42) Zheng, K.; Wen, Y.; Huang, B.; Wang, J.; Chen, J.; Xie, G.; Lv, G.; Liu, J.; Qiao, Z.; Yang, G. The solid phase thermal decomposition and nanocrystal effect of hexahydro-1,3,5-trinitro-1,3,5-triazine (RDX) via ReaxFF large-scale molecular dynamics simulation. *Phys. Chem. Chem. Phys.* **2019**, *21*, 17240–17252.
- (43) Khichar, M.; Patidar, L.; Thynell, S. Comparative Analysis of Vaporization and Thermal Decomposition of Cyclotrimethylenetrinitramine (RDX). *J. Propul. Power* **2019**, *35*, 1098–1107.
- (44) Singh, S. K.; La Jeunesse, J.; Vuppuluri, V.; Son, S. F.; Sun, B.-J.; Chen, Y.-L.; Chang, A. H. H.; Mebel, A. M.; Kaiser, R. I. The elusive ketene ( $\text{H}_2\text{CCO}$ ) channel in the infrared multiphoton dissociation of solid 1,3,5-trinitro-1,3,5-triazine (RDX). *ChemPhysChem* **2020**, *21*, 837–842.
- (45) Kuklja, M. M.; Aduiev, B. P.; Aluker, E. D.; Krashenin, V. I.; Krechetov, A. G.; Mitrofanov, A. Y. Role of electronic excitations in explosive decomposition of solids. *J. Appl. Phys.* **2001**, *89*, 4156–4166.
- (46) Bhattacharya, A.; Guo, Y.; Bernstein, E. R. Nonadiabatic reaction of energetic molecules. *Acc. Chem. Res.* **2010**, *43*, 1476–1485.
- (47) Akin, F. A. Ionisation energy, electron affinity, and mass spectral decomposition mechanisms of RDX isomers upon electron attachment and electron ionisation. *Mol. Phys.* **2016**, *114*, 3556–3566.
- (48) Cooper, J.; Zhang, J.; Grant, C. Ab initio calculation of ionization potential and electron affinity of six common explosive compounds. *Rep. Theor. Chem.* **2012**, *1*, 11–19.
- (49) Orloff, M. K.; Mullen, P. A.; Rauch, F. C. Molecular orbital study of the electronic structure and spectrum of hexahydro-1,3,5-trinitro-s-triazine. *J. Phys. Chem.* **1970**, *74*, 2189–2192.
- (50) Borges, I., Jr; Aquino, A. J. A.; Barbatti, M.; Lischka, H. The electronically excited states of RDX (hexahydro-1,3,5-trinitro-1,3,5-triazine): Vertical excitations. *Int. J. Quantum Chem.* **2009**, *109*, 2348–2355.
- (51) Zhang, T.; Cheng, L.; Zhang, J.; Wang, K. CPMD Investigation of  $\alpha$ -RDX and  $\epsilon$ -CL-20: The transition of deflagration to detonation depending on the self-produced radicals. *Phys. Chem. Chem. Phys.* **2020**, *22*, 7421–7429.
- (52) Xiong, Y.; Ma, Y.; He, X.; Xue, X.; Zhang, C. Reversible intramolecular hydrogen transfer: A completely new mechanism for low impact sensitivity of energetic materials. *Phys. Chem. Chem. Phys.* **2019**, *21*, 2397–2409.
- (53) Bennett, C. J.; Brotton, S. J.; Jones, B. M.; Misra, A. K.; Sharma, S. K.; Kaiser, R. I. High-sensitivity raman spectrometer to study pristine and irradiated interstellar ice analogs. *Anal. Chem.* **2013**, *85*, 5659–5665.
- (54) Jones, B. M.; Kaiser, R. I. Application of reflectron time-of-flight mass spectroscopy in the analysis of astrophysically relevant ices exposed to ionization radiation: Methane ( $\text{CH}_4$ ) and D4-Methane ( $\text{CD}_4$ ) as a case Study. *J. Phys. Chem. Lett.* **2013**, *4*, 1965–1971.
- (55) Bergantini, A.; Abplanalp, M. J.; Pokhilkov, P.; Krylov, A. I.; Shingledecker, C. N.; Herbst, E.; Kaiser, R. I. A combined experimental and theoretical study on the formation of interstellar propylene oxide ( $\text{CH}_3\text{CHCH}_2\text{O}$ )—A chiral molecule. *Astrophys. J.* **2018**, *860*, 108.
- (56) Isbell, R. A.; Brewster, M. Q. Optical properties of energetic materials: RDX, HMX, AP, NC/NG, and HTPB. *Propellants, Explos., Pyrotech.* **1998**, *23*, 218–224.
- (57) Bennett, C. J.; Jamieson, C.; Mebel, A. M.; Kaiser, R. I. Untangling the formation of the cyclic carbon trioxide isomer in low temperature carbon dioxide ices. *Phys. Chem. Chem. Phys.* **2004**, *6*, 735–746.
- (58) Feagin, T. A.; Rae, P. J. Optical absorption in polycrystalline PETN, RDX, HMX, CL-20 and HNS and its possible effect on exploding bridgewire detonator function. *J. Energ. Mater.* **2020**, 1–11.
- (59) Szymańczyk, M. S. a. L. Analysis of common explosives in different solvents by nuclear magnetic resonance spectroscopy. *Cent. Eur. J. Energy Mater.* **2014**, *11*, 129–142.
- (60) Infante-Castillo, R.; Pacheco-Londoño, L.; Hernández-Rivera, S. P. Vibrational spectra and structure of RDX and its  $^{13}\text{C}$ - and  $^{15}\text{N}$ -labeled derivatives: A theoretical and experimental study. *Spectrochim. Acta, Part A* **2010**, *76*, 137–141.
- (61) Iqbal, Z.; Suryanarayanan, K.; Bulusu, S.; Autera, J. R. *Infrared and Raman Spectra of 1,3,5-trinitro-1,3,5-triazacyclohexane (RDX)* **1972**, DOI: 10.21236/AD0752899.
- (62) Zheng, W.; Jewitt, D.; Kaiser, R. I. Formation of hydrogen, oxygen, and hydrogen peroxide in electron-irradiated crystalline water ice. *Astrophys. J.* **2006**, *639*, 534–548.
- (63) Kagann, R. H.; Maki, A. G. Infrared absorption intensities of nitrous acid (HONO) fundamental bands. *J. Quant. Spectrosc. Radiat. Transfer* **1983**, *30*, 37–44.
- (64) Socrates, G. *Infrared and Raman characteristic group frequencies; Tables and charts*, 3rd ed.; John Wiley and Sons, Ltd: Chichester, U.K., 2001.
- (65) Góbi, S.; Crandall, P. B.; Maksyutenko, P.; Förstel, M.; Kaiser, R. I. Accessing the nitromethane ( $\text{CH}_3\text{NO}_2$ ) potential energy surface in methanol ( $\text{CH}_3\text{OH}$ )—nitrogen monoxide (NO) ices exposed to ionizing radiation: An FTIR and PI-ReTOF-MS investigation. *J. Phys. Chem. A* **2018**, *122*, 2329–2343.
- (66) Bibart, C. H.; Ewing, G. E. Vibrational spectrum of gaseous  $\text{N}_2\text{O}_3$ . *J. Chem. Phys.* **1974**, *61* (4), 1293–1299.
- (67) Patidar, L.; Thynell, S. T. Quantum mechanics investigation of initial reaction pathways and early ring-opening reactions in thermal decomposition of liquid-phase RDX. *Combust. Flame* **2017**, *178*, 7–20.
- (68) Mebel, A. M.; Lin, M. C.; Melius, C. F. Rate constant of the  $\text{HONO} + \text{HONO} \rightarrow \text{H}_2\text{O} + \text{NO} + \text{NO}_2$  reaction from ab initio MO and TST calculations. *J. Phys. Chem. A* **1998**, *102*, 1803–1807.
- (69) Dixon, R. N.; Rieley, H. State-selected photodissociation dynamics of  $\text{HONO}(\bar{A} \ 1A')$ : Characterization of the NO fragment. *J. Chem. Phys.* **1989**, *91*, 2308–2320.
- (70) Amarasinghe, C.; Kamasah, A.; Foley, C. D.; Thompson, J. O. F.; Suits, A. G. Imaging the photodissociation dynamics of nitrous

acid (HONO): The role of torsion. *J. Phys. Chem. A* **2017**, *121*, 7503–7510.

(71) Rook, F. L. Preparation, vapor pressure, and infrared spectrum of methyl nitrite. *J. Chem. Eng. Data* **1982**, *27*, 72–73.

(72) Bennett, C. J.; Chen, S. H.; Sun, B. J.; Chang, A. H. H.; Kaiser, R. I. Mechanical studies on the irradiation of methanol in extraterrestrial ices. *Astrophys. J.* **2007**, *660*, 1588–1608.

(73) dos Santos, M. V. P.; Proenza, Y. G.; Longo, R. L. PICVib: an accurate, fast and simple procedure to investigate selected vibrational modes and evaluate infrared intensities. *Phys. Chem. Chem. Phys.* **2014**, *16*, 17670–17680.

(74) Stirling, A.; Pápai, I.; Mink, J.; Salahub, D. R. Density functional study of nitrogen oxides. *J. Chem. Phys.* **1994**, *100*, 2910–2923.

(75) Gerakines, P. A. S.; Schutte, W. A.; Greenberg, J. M.; van Dishoeck, E. F. The infrared band strengths of H<sub>2</sub>O, CO and CO<sub>2</sub> in laboratory simulations of astrophysical ice mixtures. *Astron. Astrophys.* **1995**, *296*, 810–818.

(76) Lossing, F. P.; Lam, Y.-T.; Maccoll, A. Gas phase heats of formation of alkyl immonium ions. *Can. J. Chem.* **1981**, *59*, 2228–2231.

(77) Dibeler, V. H.; Walker, J. A.; Liston, S. K. Mass spectrometric study of photoionization. VII. Nitrogen dioxide and nitrous oxide. *J. Res. Natl. Bur. Stand., Sect. A* **1967**, *71A*, 371–378.

(78) Schroeder, M. A., Critical analysis of nitramine decomposition data: Product distributions from HMX and RDX decomposition. *18<sup>th</sup> JANNAF Meeting*; Chemical Propulsion Information Agency, 1981; Vol. 347, II, pp 395–414.

(79) Akin, F. A. Mass spectral decomposition mechanisms of RDX isomers upon electron attachment and electron ionisation: A DFT study of normal mode activation incorporating Duschinsky rotations. *Mol. Phys.* **2016**, *114*, 3277–3293.

(80) Yinon, J.; Harvan, D. J.; Hass, J. R. Mass spectral fragmentation pathways in RDX and HMX. A mass analyzed ion kinetic energy spectrometric/collisional induced dissociation study. *Org. Mass Spectrom.* **1982**, *17*, 321–326.

(81) Farber, M.; Srivastava, R. D. Mass spectrometric investigation of the thermal decomposition of RDX. *Chem. Phys. Lett.* **1979**, *64*, 307–310.

(82) Darnez, C.; Paviot, J. Mise en évidence par R.P.E. d'espèces intermédiaires radicalaires intervenant dans la décomposition de quelques nitramines irradiées. *Int. J. Radiat. Phys. Chem.* **1972**, *4*, 11–23.

(83) Pace, M. D.; Britt, A. D.; Moniz, W. B. EPR investigations of thermal decomposition of nitramines: I. primary nitroxide radicals from RDX. *J. Energ. Mater.* **1983**, *1*, 127–132.

(84) Abplanalp, M. J.; Góbi, S.; Kaiser, R. I. On the formation and the isomer specific detection of methylacetylene (CH<sub>3</sub>CCH), propene (CH<sub>3</sub>CHCH<sub>2</sub>), cyclopropane (c-C<sub>3</sub>H<sub>6</sub>), vinylacetylene (CH<sub>2</sub>CHCCH), and 1,3-butadiene (CH<sub>2</sub>CHCHCH<sub>2</sub>) from interstellar methane ice analogues. *Phys. Chem. Chem. Phys.* **2019**, *21*, 5378–5393.

(85) Singh, S. K.; Tsai, T.-Y.; Sun, B.-J.; Chang, A. H. H.; Mebel, A. M.; Kaiser, R. I. Gas phase identification of the elusive N-Hydroxyoxaziridine (c-H<sub>2</sub>CON(OH)): A chiral molecule. *J. Phys. Chem. Lett.* **2020**, *11*, 5383–5389.